Characterization of Suspended Particle Size Distribution in Global Highly Turbid Waters From VIIRS Measurements

Wei Shi[1,2] and **Menghua Wang[1]**

[1]Center for Satellite Applications and Research, NOAA National Environmental Satellite, Data, and Information Service, College Park, MD, USA, [2]CIRA, Colorado State University, Fort Collins, CO, USA

Abstract Normalized water-leaving radiance spectra $nL_w(\lambda)$ at the near-infrared (NIR) bands from six years of observations (2012–2017) with the Visible Infrared Imaging Radiometer Suite (VIIRS) on-board the Suomi National Polar-orbiting Partnership are used to derive both the power law slope η of the particle backscattering coefficient spectra $b_{bp}(\lambda)$ and the particle size power law slope ξ for turbid coastal and inland waters. Based on the fact that the absorption coefficient of sea water $a_w(\lambda)$ is generally much larger than those of the other constituents $a_{iop}(\lambda)$ at the NIR wavelengths in coastal and inland waters, a NIR-based $b_{bp}(\lambda)$ algorithm for turbid waters has been used to derive the power law slope η. A three-order polynomial function between η and ξ in Kostadinov et al. (2009, https://doi.org/10.1029/2009JC005303) is applied to calculate the particle size slope ξ. Seasonal and interannual variations of η and ξ in China's east coastal region, the Amazon River Estuary, the La Plata River Estuary, the Meghna River Estuary, and the Atchafalaya River Estuary are characterized and quantified. Except for the Amazon River Estuary, η and ξ have significant seasonal dependence in these highly turbid regions. Among the global highly turbid waters, the Meghna River Estuary shows the most significant seasonal variations in η and ξ with the largest particle size in the surface layer. The peaks of the climatology η and ξ are at ~ −1.2 and 3.2 in the Meghna River Estuary, respectively. Particle size parameters η and ξ are also shown to be related to the magnitude of $nL_w(\lambda)$ (or $b_{bp}(\lambda)$) at the NIR bands with strong regional dependence. This study demonstrates that η and ξ increase from the inshore to offshore regions in these highly turbid waters, illustrating the more large particles in the inshore waters than the offshore ocean regions. In addition, wind and precipitation data in the Amazon River Estuary and Meghna River Estuary show that wind forcing is the major driver for the particle size distribution dynamics in these highly turbid water regions.

1. Introduction

Suspended marine particles in the ocean are important constituents in the water column that are related to many ocean physical, geochemical, and biological processes, such as phytoplankton blooms, flocculation, aggregation, and sediment resuspension (Dyer et al., 2000; Pannard et al., 2007; Wang et al., 2013). Particle size in the seawater is critical in characterizing the marine ecosystem, phytoplankton community, and phytoplankton function type (Falkowski et al., 1998; Hood et al., 2006; Le Quere et al., 2005). The particle settling velocity is strongly impacted by the particle size (Ahn, 2012; Mccave, 1975). The light penetration, scattering, and attenuation in seawater are also affected by the particle size (Babin et al., 2003; Baker & Lavelle, 1984). Thus, particle size distribution (PSD) plays an important role in modeling biogeochemical processes for the global ocean as well as for assessing the ocean ecosystem dynamics and the ocean's carbon cycle (Falkowski et al., 1998; Le Quere et al., 2005; Maranon, 2015).

Unlike the open ocean, coastal regions, particularly the highly turbid regions like river estuaries, are dominated with inorganic materials such as clays, silts, and fine sands from the bottom or from the river flows (Bowers & Binding, 2006). Suspended particles in coastal and estuarine waters are commonly in the form of the aggregates or flocs (Eisma et al., 1990), and the particulate aggregation can affect the beam attentuation (Boss et al., 2009). The physical and biogeochemical processes such as seasonal climate changes, wind-driven turbulence, tidal current, and waves can change the PSD in coastal and estuarine waters (Ellis et al., 2004; Renosh et al., 2014; Renosh et al., 2015; Wolanski & Gibbs, 1995). Thus, studying the dynamics, spatial and temporal variability of PSD, and its roles on the physical and biogeochemical processes in coastal and estuarine waters can provide a better understanding of global and regional marine ecosystems.

The particle size in the ocean water column can have a wide range from a few microns in radius to over ~100 µm (Bowers et al., 2007; Buonassissi & Dierssen, 2010; Qiu et al., 2016; Xi et al., 2014). Several mathematical models have been proposed to approximate the PSD shape in the marine environment (Ceronio & Haarhoff, 2005; Jonasz, 1987; Junge, 1963; Kitchen et al., 1975; Boss et al., 2011; Risovic, 1993). Even though particle size distributions in natural waters are usually much more complex, various studies and in situ investigations found that the Junge type (or power law) PSD (Junge, 1963) and the power law approximation generally provide a good fit to the surface ocean particle size distributions with particle size measurements that span from a few microns to ~100 µm (Buonassissi & Dierssen, 2010; Qiu et al., 2016; Sheldon et al., 1972; Twardowski et al., 2001).

The PSD in the marine environments is related to the particle backscattering spectra (Boss et al., 2001; Kostadinov et al., 2009; Loisel et al., 2006; Morel, 1973). Slade and Boss (2015) showed that spectral backscattering contains information of the average particle size from the in situ measurements. The power law slope ξ of the PSD can be derived from the power law slope η of the particle backscattering coefficient spectra $b_{bp}(\lambda)$ with the assumptions that the PSD in the marine environment is in the power law distribution and water absorption at the near-infrared (NIR) wavelengths is significantly larger than that of other inherent optical property (IOP) components. Thus, it is natural to characterize and quantify the global marine PSD with the particle backscattering coefficients $b_{bp}(\lambda)$ from satellite ocean color remote sensing. A general decrease of the $b_{bp}(\lambda)$ spectral slope from the oligotrophic oceans to eutrophic waters is observed (Loisel et al., 2006). Correspondingly, subtropical oligotrophic gyres are characterized with high PSD slopes and low particle number concentrations in comparison with coastal eutrophic regions. The picoplankton-size particles dominate the oligotrophic waters, while eutrophic waters are generally featured with high number concentrations of microplankton-size particles (Kostadinov et al., 2009) as compared to the open ocean. In turbid coastal and estuarine waters, suspended particles are mainly from suspended sediments, and particle size generally decreases from the inshore to offshore regions (Park et al., 2001; Xi et al., 2014).

Unlike open ocean waters, the normalized water-leaving radiance spectra $nL_w(\lambda)$ in the coastal turbid region are significantly enhanced at the spectral range of the red and NIR bands (Arnone et al., 1998; Knaeps et al., 2015; Ruddick et al., 2006; Shi & Wang, 2014; Stumpf et al., 2003; Wang et al., 2007; Wang et al., 2011). Thus, accurate retrievals of $nL_w(\lambda)$ spectra at the red and NIR bands from the shortwave infrared (SWIR)-based atmospheric correction algorithms (Wang, 2007; Wang & Shi, 2007) provide further optical information about the ocean (water) beyond traditional blue and green wavelengths to address the complexity of coastal and inland turbid waters. Based on the spectral features of the IOP constituents in the ocean, it is demonstrated that a NIR-based $b_{bp}(\lambda)$ algorithm can derive $b_{bp}(\lambda)$ products in highly turbid coastal and inland waters with good accuracy (Shi & Wang, 2014, 2017). In fact, $b_{bp}(\lambda)$ can reach over ~3–4 m^{-1} in the Amazon River Estuary and China's east coastal region (Shi & Wang, 2017). In addition, $b_{bp}(\lambda)$ spectra in different highly turbid regions are also seasonal and regional dependent, attributed to the different particle size distributions in these waters (Shi & Wang, 2017).

In this study, we use $nL_w(\lambda)$ spectra at the NIR bands of 745 and 862 nm derived from the SWIR-based atmospheric correction algorithm (Wang, 2007) with observations from the Visible Infrared Imaging Radiometer Suite (VIIRS) on-board the Suomi National Polar-orbiting Partnership (SNPP) between 2012 and 2017 to compute $b_{bp}(\lambda)$ in the two NIR bands for major highly turbid waters. Different from the Shi and Wang (2017) study to characterize the particle backscattering of global highly turbid waters, the power law slope η of the $b_{bp}(\lambda)$ spectra is computed from $b_{bp}(\lambda)$ in the two NIR bands, and the slope ξ of the PSD is further computed analytically from the parameter η following the formula in Kostadinov et al. (2009). We analyze the spatial and temporal variations of ξ in these regions. The comparison of the satellite-derived PSD slope ξ and results from other studies, including possible uncertainties of the PSD retrievals and the PSD dynamics in these highly turbid water regions, are also discussed.

2. Methods and Data

2.1. VIIRS-SNPP Data Over Global Highly Turbid Water Regions

VIIRS is one of the key instruments on board the SNPP satellite, which was launched on 28 October 2011. VIIRS has similar spectral bands to the Moderate Resolution Imaging Spectroradiometer (MODIS) that
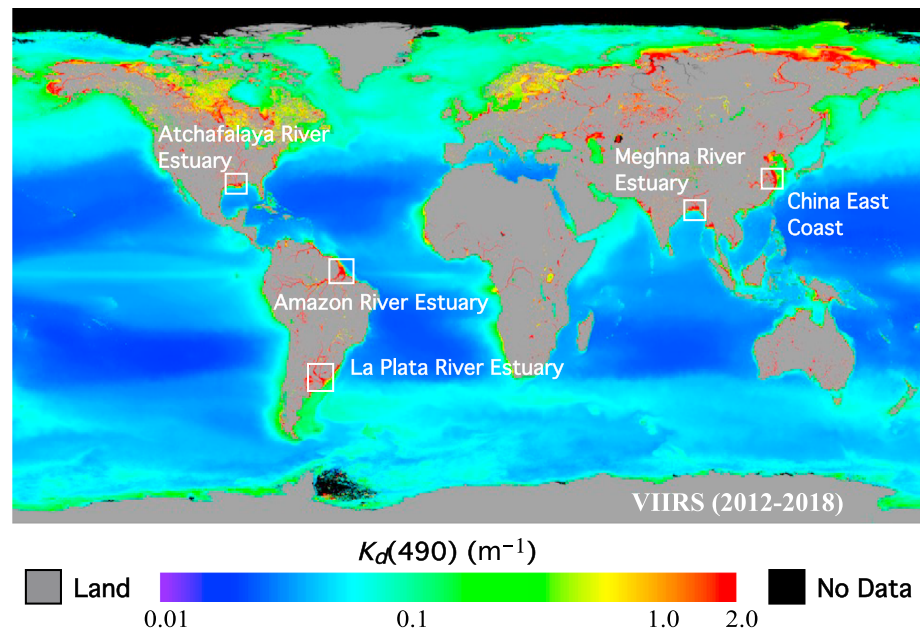
Figure 1. Global climatology $K_d(490)$ distribution derived from Visible Infrared Imaging Radiometer Suite observations between 2012 and 2018. The turbid water regions in this study are marked for the China East Coast, Amazon River Estuary, La Plata River Estuary, Meghna River Estuary, and Atchafalaya River Estuary.

provides observations of Earth's atmosphere, land, and ocean properties (Goldberg et al., 2013). One of the primary goals of the VIIRS mission is to provide the data continuity from MODIS for the science and user communities with the Environmental Data Records (EDR or Level-2 data) over global oceanic waters to enable assessment of climatic and environmental variability (McClain, 2009). Ocean color EDR is one of several key product suites derived from VIIRS (Wang, Liu, et al., 2013).

Specifically, VIIRS-SNPP has moderate spatial resolution (750 m) of five visible bands (M1–M5) with nominal central wavelengths of 410, 443, 486, 551, and 671 nm, two NIR bands (M6 and M7) at the wavelengths of 745 and 862 nm, and the three SWIR bands (M8, M10, and M11) at the wavelengths of 1,238, 1,601, and 2,257 nm, as well as three imaging bands (I1–I3) with spatial resolution (375 m) at 638, 862, and 1,600 nm, for satellite ocean color data processing (Wang et al., 2016; Wang & Jiang, 2018; Wang, Liu, et al., 2013). On-orbit vicarious calibration for VIIRS-SNPP was carefully carried out using the in situ $nL_w(\lambda)$ spectra from the Marine Optical Buoy (Clark et al., 1997) in the waters off Hawaii and over the South Pacific Gyre (Wang et al., 2016).

2.2. The $nL_w(\lambda)$ Spectra Derived From the SWIR-Based Ocean Color Data Processing

Satellite measurements at the two MODIS or VIIRS SWIR bands can be used to derive $nL_w(\lambda)$ spectra from the visible to NIR and SWIR 1,240-nm band (Shi & Wang, 2009; Wang, 2007; Wang & Shi, 2007). The Multi-Sensor Level-1 to Level-2 (MSL12) ocean color data processing system (Wang, 1999; Wang & Franz, 2000; Wang, Liu, et al., 2013), which is the official NOAA VIIRS ocean color data processing system, has been used for routinely processing satellite ocean color data from the Sensor Data Records (SDR or Level-1B data) to ocean color EDR (Level-2 data) products for VIIRS-SNPP. There are various atmospheric correction approaches implemented in MSL12, including the NIR-SWIR combined atmospheric correction algorithm (Wang & Shi, 2007; Gordon & Wang, 1994; Wang, 2007; Wang, Son, Shi, 2009). In this study, climatology and seasonal composites of remapped VIIRS $nL_w(\lambda)$ spectra between 2012 and 2017 derived using the NIR-SWIR algorithm (Wang & Shi, 2007; Gordon & Wang, 1994; Wang, 2007; Wang, Son, Shi, 2009) in turbid regions, including China's East Coast, the Amazon River Estuary, the La Plata River Estuary between Uruguay and Argentina, the Meghna River Estuary in the Bay of Bengal, and the Atchafalaya River Estuary in distributaries of the Mississippi River, were used to produce $b_{bp}(\lambda)$, $b_{bp}(\lambda)$ power law slope η, and PSD slope ξ. Figure 1 shows global climatology diffuse attenuation coefficient at the wavelength of 490 nm $K_d(490)$ (Wang, Son, Harding, 2009) derived from the VIIRS observations (2012–2018) with the

locations of these turbid regions marked. While $K_d(490)$ is generally less than 0.1 m^{-1} for the global open ocean, $K_d(490)$ in these turbid regions are all over 2 m^{-1}.

2.3. The NIR-Based $b_{bp}(\lambda)$, η, and ξ Algorithms for VIIRS Ocean Color Observations

Satellite-measured $nL_w(\lambda)$ data are intrinsically related to the water constituents such as colored dissolved organic matter, phytoplankton particles, and inorganic sediments (Gordon et al., 1988). Gordon et al. (1988) developed a quadratic model between the remote sensing reflectance just beneath the ocean surface $r_{rs}(\lambda)$ and ocean's IOPs, that is,

$$r_{rs}(\lambda) = g_1 \left(\frac{b_b(\lambda)}{a(\lambda) + b_b(\lambda)} \right) + g_2 \left(\frac{b_b(\lambda)}{a(\lambda) + b_b(\lambda)} \right)^2, \tag{1}$$

where g_1 and g_2 are constant values of 0.0949 and 0.0794 sr^{-1} as derived in Gordon et al. (1988). It is noted that $r_{rs}(\lambda)$ can be directly converted from $nL_w(\lambda)$ (Lee et al., 1999). It should also be noted that equation (1) works for both the open ocean and coastal turbid waters. Coefficients $a(\lambda)$ and $b_b(\lambda)$ in equation (1) are total absorption and backscattering coefficients, respectively, which can be expressed as

$$a(\lambda) = a_w(\lambda) + a_{ph}(\lambda) + a_g(\lambda) + a_d(\lambda), \tag{2}$$

$$b_b(\lambda) = b_{bw}(\lambda) + b_{bp}(\lambda), \tag{3}$$

where $a_w(\lambda)$, $a_{ph}(\lambda)$, $a_g(\lambda)$, and $a_d(\lambda)$ are absorption coefficients for pure seawater, phytoplankton, dissolved matter, and nonalgal particles, respectively, and $b_{bw}(\lambda)$ and $b_{bp}(\lambda)$ are backscattering coefficients for pure seawater and particulate matters, respectively.

In fact, $a_d(\lambda)$ and $b_{bp}(\lambda)$ are related to the particle concentration, particle size distribution, particle backscattering ratio, particle refractive index, etc. Furthermore, $b_{bp}(\lambda)$ is normally proportional to the particle concentration to the first order, while particle size and particle backscattering ratio are associated to the $b_{bp}(\lambda)$ spectrum. In recent studies, Shi and Wang (2014, 2017) developed a NIR-based IOP algorithm to retrieve $b_{bp}(\lambda)$ in coastal and inland turbid waters based on the spectral features of the absorptions of pure seawater $a_w(\lambda)$, phytoplankton $a_{ph}(\lambda)$, dissolved matters $a_g(\lambda)$, and nonalgal particles absorption $a_d(\lambda)$ at the NIR wavelengths. Briefly, pure seawater absorption coefficients $a_w(\lambda)$ at the NIR bands are typically significantly higher than those from other constituents, that is, $a_w(\lambda) >> a_{ph}(\lambda)$, $a_g(\lambda)$, and $a_d(\lambda)$. For example, $a_w(862)$ is ~5 m^{-1} as compared to $a_{ph}(\lambda)$, $a_g(\lambda)$, and $a_d(\lambda)$ at 862 nm that are normally negligible in comparison with $a_w(862)$. Therefore, with the spectral features of $a_w(\lambda)$, $a_{ph}(\lambda)$, $a_g(\lambda)$, and $a_d(\lambda)$ at the VIIRS NIR 745- and 862-nm bands, $b_b(\lambda)/(a(\lambda) + b_b(\lambda))$ can be approximated as

$$\left(\frac{b_b(\lambda)}{a(\lambda) + b_b(\lambda)} \right) \approx \left(\frac{b_b(\lambda)}{a_w(\lambda) + b_b(\lambda)} \right). \tag{4}$$

In equation (3), $b_{bp}(\lambda)$ is spectrally correlated, and can be generally modeled as a function of $b_{bp}(\lambda)$ at a reference wavelength (Gordon & Morel, 1983; IOCCG, 2006), that is, $b_{bp}(\lambda_0)$, with a power law slope η. The function can be expressed as

$$b_{bp}(\lambda) = b_{bp}(\lambda_0) \left(\frac{\lambda_0}{\lambda} \right)^{\eta}. \tag{5}$$

In this study, $b_{bp}(745)$ and $b_{bp}(862)$ are derived from VIIRS-measured $nL_w(745)$ and $nL_w(862)$ using MSL12 with the SWIR-based atmospheric correction in turbid waters. The power law slope η can then be consequently computed from equation (5) with known $b_{bp}(745)$ and $b_{bp}(862)$ as the reference $b_{bp}(\lambda_0)$.

The Junge type (or power law) PSD (Boss et al., 2001; Junge, 1963) in the marine environments can be expressed in the following equation:

$$N(D) = N_0 \left(\frac{D_0}{D} \right)^{\xi}, \tag{6}$$

where N_0 is the number of particles per volume normalized by the size bin width in units of meter^{-4} at the reference particle size D_0, and N is the number of particles per volume normalized by the size bin width at a

certain particle size D, and ξ is the power law slope. In this study, the slope ξ is used to characterize the particle size distributions in highly turbid waters. Low values of ξ (e.g., $\xi = 3.0$ and below) represent more large particles in the PSD spectrum than the high values of ξ (e.g., $\xi = 4.0$ and above). Power law slope η is related to the power law slope of PSD, that is, $\xi \approx \eta + 3$ (Babin et al., 2003; Kostadinov et al., 2009; Morel, 1973) with the assumption that the particle size follows the power law distribution and the spectrum of $b_{bp}(\lambda)$ follows a power law relationship as shown in equation (5). Even though particle backscattering properties are functions of the PSD, particle shapes, and composition, etc., PSD is a major factor in determining the particle scattering features such as the backscattering power law slope and the backscattering ratio (Kostadinov et al., 2009; Ulloa et al., 1994). The impact of PSD depends on a couple of the optical properties such as the index of refraction and PSD slope (Mobley et al., 2002; Twardowski et al., 2001). The relationship between η and ξ can be mathematically expressed in a three-degree polynomial fit for wide ranges of η and ξ with good accuracy over the 490-, 510-, and 555-nm bands (Kostadinov et al., 2009) after extensive Mie scattering simulations (Mie, 1908), that is,

$$\xi = -0.00191\eta^3 + 0.127\eta^2 + 0.482\eta + 3.52. \tag{7}$$

Note that equation (7) is a fit to a look-up-table, not a physical formula. Using equation (7), the power law slope η derived from $b_{bp}(745)$ and $b_{bp}(862)$ is converted to the power law slope ξ of the PSD in coastal turbid waters. Following the procedure as described in equations (1)–(4), $b_{bp}(745)$ and $b_{bp}(862)$ derived from VIIRS-SNPP observations were produced to characterize the dynamics of the $b_{bp}(\lambda)$ power law slope η and the PSD power law slope ξ in global highly turbid coastal and inland waters.

3. Results

3.1. VIIRS-Derived $nL_w(\lambda)$ and $b_{bp}(\lambda)$ at the NIR Bands in Highly Turbid Waters

In highly turbid waters, ocean optical properties are characterized by enhanced $nL_w(\lambda)$ in the red and NIR wavelengths (Doron et al., 2011; Doxaran et al., 2002; Shi & Wang, 2014). Five moderately to highly turbid regions (Shi & Wang, 2010) are selected for this study. These five regions shown in Figure 1 include (1) China's east coastal region, (2) Amazon River Estuary, (3) La Plata River Estuary, (4) Meghna River Estuary in the Bay of Bengal, and (5) Atchafalaya River Estuary in the distributaries of the Mississippi River. Of the five selected regions, Atchafalaya River Estuary is the only moderately turbid region.

Figure 2 shows the climatology of VIIRS-derived $nL_w(745)$ from the daily VIIRS observations (Figures 2a–2e) and $nL_w(862)$ (Figures 2f–2j) between 2012 and 2017 in these five regions. Indeed, these regions are featured with significantly enhanced $nL_w(745)$ and $nL_w(862)$. Specifically, $nL_w(745)$ and $nL_w(862)$ can reach over ~4–5 and ~2–3 mW·cm^{-2}·μm^{-1}·sr^{-1}, respectively, in some areas of China's east coastal region (Figures 2a and 2f) and the Amazon River Estuary (Figures 2b and 2g). The La Plata River Estuary (Figures 2c and 2h) and the Meghna River Estuary (Figures 2d and 2i) are less turbid than the Amazon River Estuary in terms of $nL_w(745)$ and $nL_w(862)$ magnitudes. The Atchafalaya River Estuary in distributaries of the Mississippi River is the least turbid water in these five regions. It is similar to many other coastal and inland turbid regions such as the northern Caspian Sea, the North Sea, and the Chesapeake Bay (Shi & Wang, 2010).

Overall, the climatology of VIIRS-derived $nL_w(745)$ and $nL_w(862)$ show that there are significant differences in terms of the magnitudes in $nL_w(745)$ and $nL_w(862)$ in highly turbid coastal and inland waters. VIIRS-derived $nL_w(745)$ and $nL_w(862)$ in these highly turbid water regions can be used to calculate particle backscattering $b_{bp}(745)$ and $b_{bp}(862)$ and characterize and quantify the $b_{bp}(\lambda)$ power law slope η and PSD slope ξ for global highly turbid waters.

Figure 2 also shows the climatology of $b_{bp}(745)$ (Figures 2k–2o) and $b_{bp}(862)$ (Figures 2p–2t) derived from VIIRS observations between 2012 and 2017. The spatial distributions of $b_{bp}(745)$ and $b_{bp}(862)$ are consistent with those of $nL_w(745)$ and $nL_w(862)$. However, they are not exactly linearly correlated. Seasonal variability of $nL_w(\lambda)$ and $b_{bp}(\lambda)$ is also significant in some of these regions (not shown here; Shi & Wang, 2017), such as China's east coastal region. Winter season is the most turbid season with enhanced $b_{bp}(\lambda)$ and enlarged coverage of high $b_{bp}(\lambda)$ in China's east coastal region, while the lowest $b_{bp}(\lambda)$ occurs in the summer season.
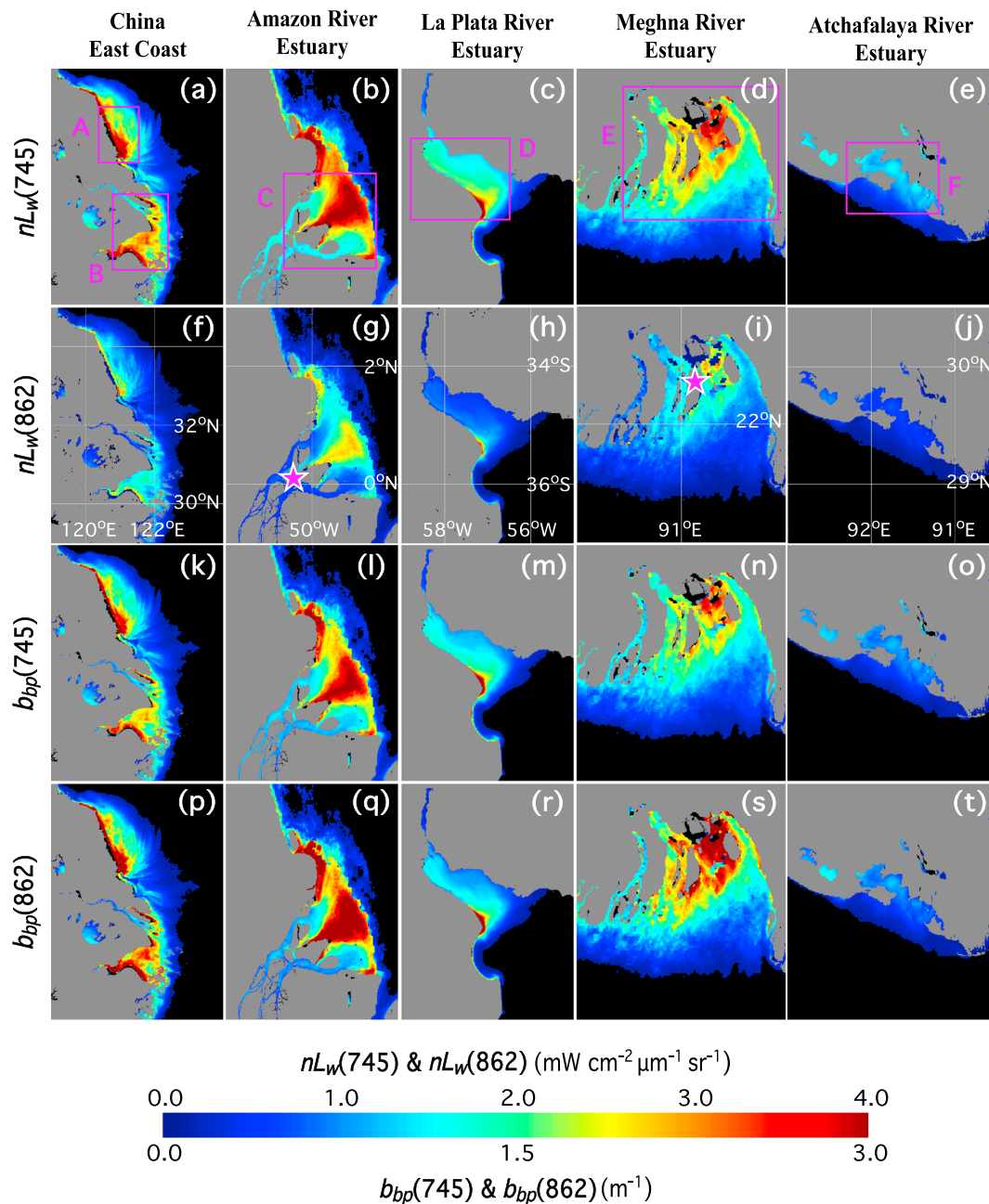
Figure 2. Visible Infrared Imaging Radiometer Suite-derived climatology $nL_w(745)$, $nL_w(862)$, $b_{bp}(745)$, and $b_{bp}(862)$ in the regions of (a, f, k, p) China's east coastal region between (29.0–35.0°N) and (119.0–124.0°E), (b, g, l, q) Amazon River Estuary between (1.0°S–3.0°N) and (52.0–48.0°W), (c, h, m, r) La Plata River Estuary between (37.0–33.0°S) and (59.0–55.0°W), (d, i, n, s) Meghna River Estuary between (21.0–23.0°N) and (90.0–92.0°E), and (e, j, o, t) Atchafalaya River Estuary between (28.5–30.5°N) and (93.0–90.5°W). The regions with $nL_w(745) < 0.2$ mW·cm^{-2}·µm^{-1}·sr^{-1} (or no retrievals) are marked in black. The latitude and longitude grids for the regions are marked in (f)–(j). The box areas for each region in (a)–(e) are marked as A–F for further analysis. Star marks in panels (g) and (i) represent the locations of the wind and rainfall data for further analysis in Figure 13.

3.2. Seasonal $b_{bp}(\lambda)$ Power Law Slope η and PSD Slope ξ
3.2.1. $b_{bp}(\lambda)$ Power Law Slope η

Figures 3–7 show the climatology of the $b_{bp}(\lambda)$ power law slope η and the seasonal η derived from VIIRS observations between 2012 and 2017 in China's east coastal region (Figures 3a–3e), the Amazon River Estuary (Figures 4a–4e), the La Plata River Estuary (Figures 5a–5e), the Meghna River Estuary (Figures 6a–6e), and the Atchafalaya River Estuary (Figures 7a–7e). Note that the regions with $nL_w(745)$
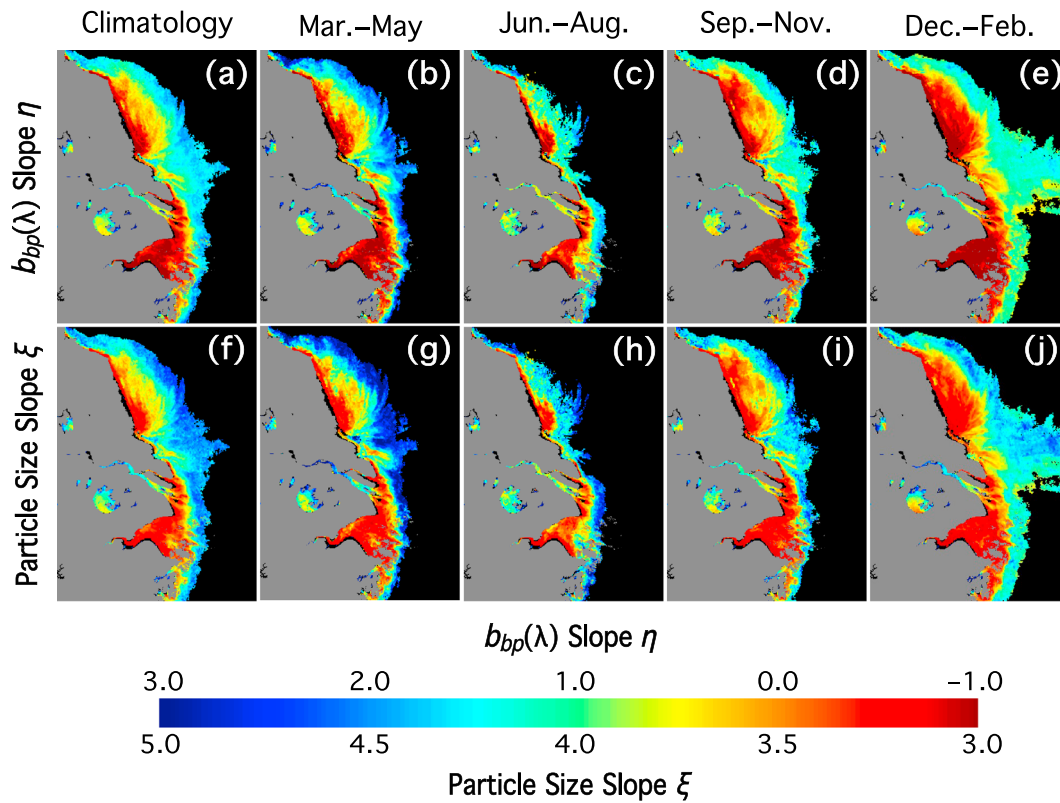
Figure 3. Visible Infrared Imaging Radiometer Suite-derived images of η and ξ in China's east coastal region for (a, f) climatology from 2012–2017, (b, g) March–May, (c, h) June–August, (d, i) September–November, and (e, j) December–February. Note η and ξ are in descending order to improve the visualization of the parameter spatial distribution in Figures 3–7. The regions with $nL_w(745) < 0.2$ mW·cm^{-2}·μm^{-1}·sr^{-1} (or no retrievals) are marked in black.

Figure 4. Visible Infrared Imaging Radiometer Suite-derived images of η and ξ in the Amazon River Estuary for (a, f) climatology from 2012–2017, (b, g) March–May, (c, h) June–August, (d, i) September–November, and (e, j) December–February. The regions with $nL_w(745) < 0.2$ mW·cm^{-2}·μm^{-1}·sr^{-1} (or no retrievals) are marked in black.
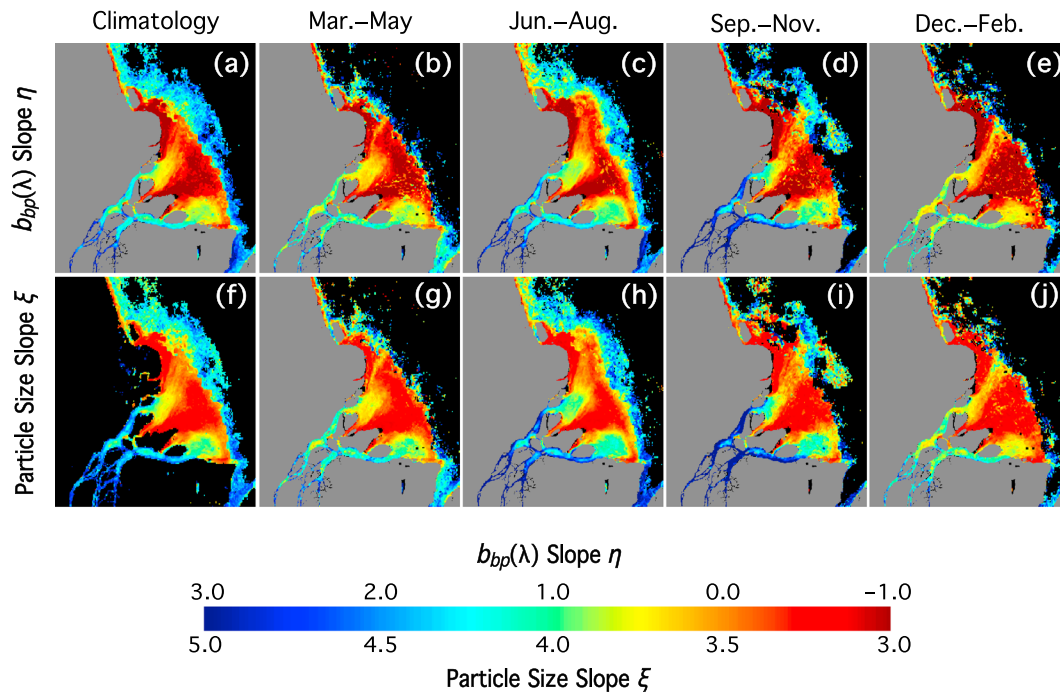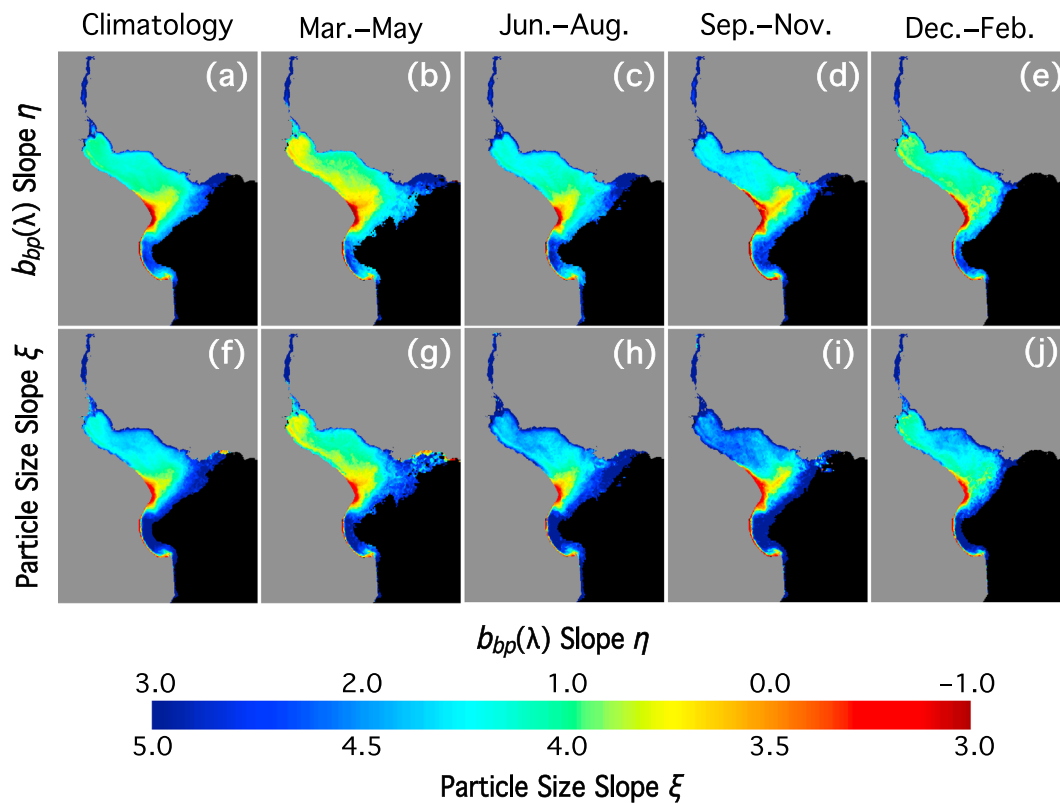
Figure 5. Visible Infrared Imaging Radiometer Suite-derived images of η and ξ in the La Plata River Estuary for (a, f) climatology from 2012–2017, (b, g) March–May, (c, h) June–August, (d, i) September–November, and (e, j) December–February. The regions with $nL_w(745) < 0.2$ mW·cm^{-2}·µm^{-1}·sr^{-1} (or no retrievals) are marked in black.
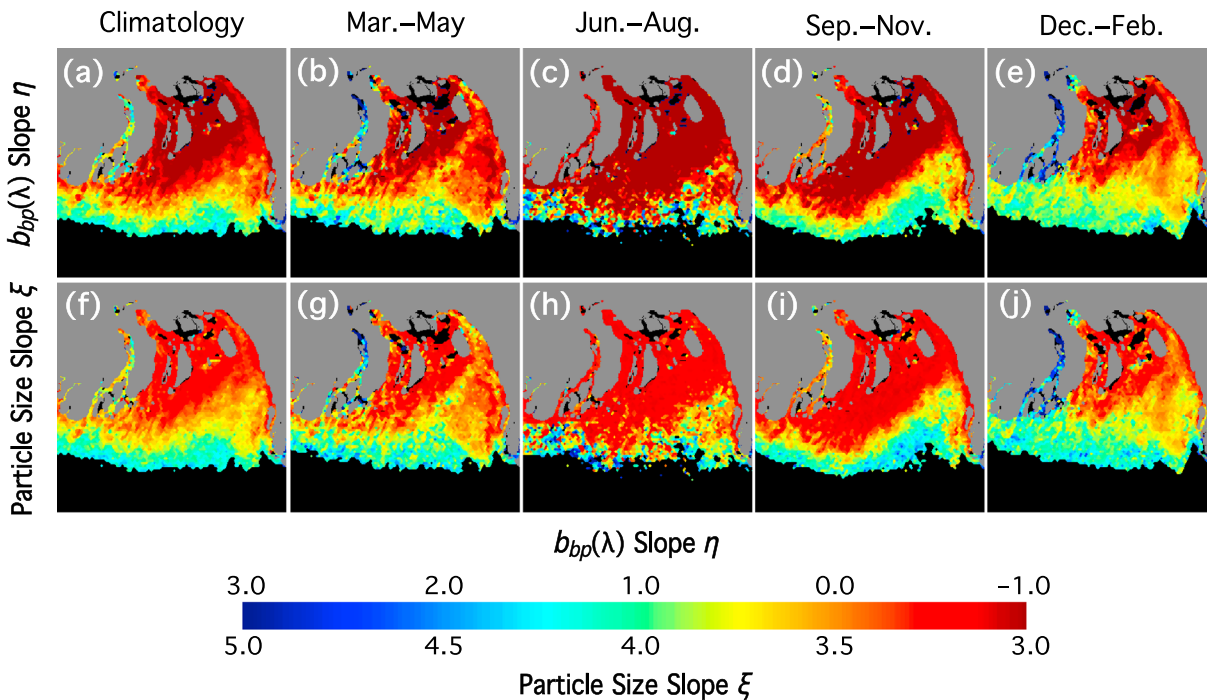

Figure 6. Visible Infrared Imaging Radiometer Suite-derived images of η and ξ in the Meghna River Estuary for (a, f) climatology from 2012–2017, (b, g) March–May, (c, h) June–August, (d, i) September–November, and (e, j) December–February. The regions with $nL_w(745) < 0.2$ mW·cm^{-2}·µm^{-1}·sr^{-1} (or no retrievals) are marked in black.
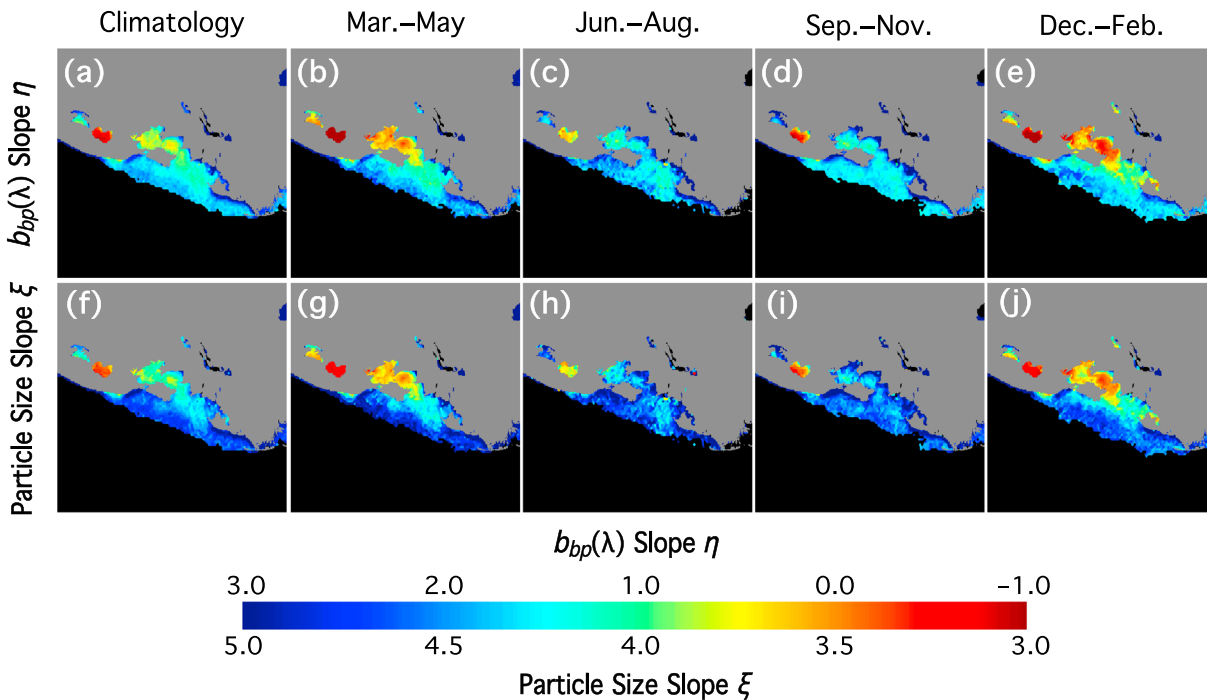
Figure 7. Visible Infrared Imaging Radiometer Suite-derived images of η and ξ in the Atchafalaya River Estuary for (a, f) climatology from 2012–2017, (b, g) March–May, (c, h) June–August, (d, i) September–November, and (e, j) December–February. The regions with $nL_w(745) < 0.2$ mW·cm^{-2}·µm^{-1}·sr^{-1} (or no retrievals) are marked in black.

< 0.2 mW·cm^{-2}·µm^{-1}·sr^{-1} are marked in black in Figures 3–7 due to high noise level in the η retrievals (Shi & Wang, 2017).

In general, negative η is located in the regions with enhanced $b_{bp}(745)$ and $b_{bp}(862)$ such as in the Subei Shoal, Yangtze River Estuary, and Hangzhou Bay of China's east coastal region (Figure 3a), while η increases in offshore regions. The seasonal variability of η is also significant in the China's east coastal region with significantly reduced η in the winter (Figure 3e). In the Subei Shoal and Hangzhou Bay, η can drop as low as below −1.0. In contrast, high η generally occurs in the summer season (Figure 3c).

Furthermore, η is below 0 in a large portion of the Amazon River Estuary (Figure 4a). There are no significant seasonal variations of η. The magnitudes of η are similar to those in China's east coastal region. In the La Plata River Estuary, the climatology η is mostly ~1.0 (Figure 5a). Unlike the Amazon River Estuary, seasonal variability of η can be found in the La Plata River Estuary. The lowest η occurs in the months of March–May (Figures 5b) with η between ~0.5 and 1.0. The highest η can be found in the months of September–November (Figures 5d) with η between ~1.0 and 1.5.

The Meghna River Estuary is featured with the lowest η at the mouth of the Meghna River, especially in the period of June–November (Figures 6c and 6d). The region of Atchafalaya River Estuary and Mississippi River Estuary is a typical turbid region similar to others like the Chesapeake Bay, the North Sea, and the Northern Caspian Sea. This region is featured with high η of ~0.5–1.0. Low η values can be found in the boreal spring and winter, while high η occurs in the summer (Figure 7c) and autumn (Figure 7d). The statistics of the η in the marked box of each region is summarized in Table 1.

3.2.2. PSD Slope ξ

The spatial distributions of ξ for PSD are consistent with the spatial patterns of η for both climatology and the seasonal distributions. Figures 3–7 also show the climatology ξ and the seasonal ξ derived from VIIRS observations between 2012 and 2017 in China's east coastal region (Figures 3f–3j), the Amazon River Estuary (Figures 4f–4j), the La Plata River Estuary (Figures 5f–5j), the Meghna River Estuary (Figures 6f–6j), and the Atchafalaya River Estuary (Figures 7f–7j).

Table 1
Statistics of Mean, Median, and Standard Deviation (STD) of η and ξ in the Six Box Regions (A–F) as Marked in Figures 2a–2e

Statistics	Subei Shoal (A)	Hanghou Bay (B)	Amazon River (C)	La Plata River (D)	Meghna River (E)	Atchafalaya River (F)
Mean η	−0.131	−0.238	0.264	1.100	−0.733	1.469
Median η	−0.004	−0.413	0.078	1.136	−0.800	1.522
STD η	0.617	0.846	1.092	0.604	0.846	0.525
Mean ξ	3.563	3.576	3.726	4.259	3.392	4.433
Median ξ	3.596	3.428	3.587	4.256	3.333	4.471
STD ξ	0.269	0.404	0.462	0.361	0.242	0.324

Highly turbid regions in China's East Coast are dominated by the particles with ξ ranging between ~3.0 and 3.5 (Figure 3f). In the farther offshore region, ξ values can go up to ~4.5. This clearly shows that the particle size decreases from coastal to offshore regions. On the other hand, significant seasonal change in the particle size can also be observed in this region. In the winter, an enlarged area of ξ between ~3.0 and 3.5 can be found in the Subei Shoal, Yangtze River Estuary, and Hangzhou Bay regions (Figure 3j). In comparison, the region covered with the large particle size shrinks significantly in the summer (Figure 3h).

On the other hand, there are no significant seasonal variations of ξ in the Amazon River Estuary. The magnitudes of ξ in the Amazon River Estuary in Figure 4 are similar to those of highly turbid regions in China's east coastal region as shown in Figure 3f. ξ values for PSD are generally larger in the La Plata River Estuary (Figure 5f). This shows that the particle size in the La Plata River Estuary is smaller than those along the China's east coastal region and in the Amazon River Estuary. ξ variations show that the particle size in the La Plata River Estuary also changes seasonally (Figures 5f–5j)

Meghna River Estuary region (Figures 6f–6j) is featured with the lowest ξ values at the mouth of the Meghna River, especially in the period of June–November. This represents the larger size particles in the Meghna River Estuary than the other regions. In this region, seasonal variations of η and ξ are significant with the lowest ξ occurring in the boreal summer and autumn season, respectively. This might be attributed to the seasonal monsoon, heavy rainfall, and high river flow in these two seasons. At the mouth of the Meghna River, ξ can reach ~3 in the summer and autumn for most of the region as compared to much higher values in the other regions.

Figure 7f shows the climatology ξ in the Atchafalaya River Estuary. Seasonal variations of ξ are also obvious. Low ξ values can be found in the boreal spring (Figure 7g) and winter (Figure 7j), while high ξ occurs in the summer (Figure 7h) and autumn (Figure 7i). This shows that this region features a larger particle size in the spring and winter in the water column, while the particle size generally is small in the summer and autumn seasons. The detail of ξ in the marked box of each region is summarized in Table 1.

3.3. Characterization and Quantification of η and ξ in Global Highly Turbid Waters

Figure 8 shows histogram distributions of the climatology η (Figure 8a) and ξ (Figure 8b) in the six boxes marked in Figure 2. Figure 8a shows that the η histograms are widely distributed from < -1.5 to $+3$ in different regions. The histogram peaks for η at the Meghna River Estuary and the Hangzhou Bay are at ~ -1.0. In the Amazon River Estuary, η peaks at ~ -0.5, and ~0 in the Subei Shoal. In the La Plata River Estuary, most of the η values are located at ~1.0. The largest η can be found in the
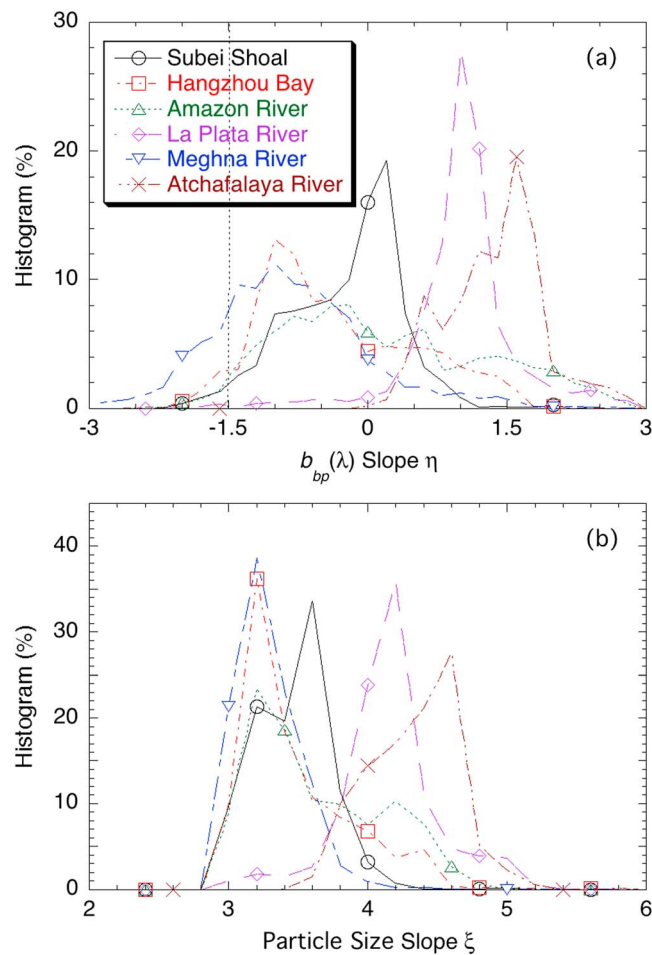

Figure 8. Histogram results derived from the six turbid regions marked in Figure 2 for (a) climatology $b_{bp}(\lambda)$ slope η and (b) climatology particle size slope ξ. A dotted line at $\eta = -1.5$ is also marked in plot (a) to show the results of the extrapolated PSD slope $\eta < -1.5$.

Atchafalaya River Estuary with the histogram peak at ~1.70. It is also noted that η distribution patterns are different. In the Amazon River Estuary, η is widely distributed between −2.0 and 3.0, while η at the La Plata River Estuary is more uniformly distributed in a narrow range. This is consistent with the climatology images of η.

For histograms of ξ in these six regions, Figure 8b clearly shows that the Meghna River Estuary, Amazon River Estuary, and Hangzhou Bay are the three regions with the largest particle size. In comparison to the Meghna River Estuary and Hangzhou Bay, the particle size in the Amazon River Estuary has a wide range with ξ from ~2.8 to 5. In the Subei Shoal, the ξ histogram peaks at ~3.6. Of the six turbid regions, the La Plata River Estuary and the Atchafalaya River Estuary are the regions with the dominance of the smallest size particles in terms of the PSD. ξ peaks at ~4.2 at the La Plata River Estuary, while the maximum ξ histogram distribution in the Atchafalaya River Estuary is ~4.6.

To further understand the seasonal changes of the PSDs in these six regions, we also computed η and ξ in each season. Figure 9 shows $b_{bp}(\lambda)$ power law slopes in (1) the Subei Shoal (Figure 9a), (2) the Hangzhou Bay (Figure 9b), (3) the Amazon River Estuary (Figure 9c), (4) the La Plata River Estuary (Figure 9d), (5) the Meghna River Estuary (Figure 9e), and (6) the Atchafalaya River Estuary (Figure 9f). Of these six regions, five regions show notable seasonal variations of η, except for the Amazon River Estuary. In the Amazon River Estuary, η distributions are similar for all the four seasons ranging from about −2.0 to 3.0. Along China's east coastal region, η in the Hangzhou Bay (Figure 9b) shows less seasonal variability than that in the Subei Shoal (Figure 9a). In both regions, the lowest η occurs in the winter season between December and February, and the highest η in the summer season between June and August. Specifically, the η peak value over the Subei Shoal varies from −1.0 in the winter to 1.0 in the summer. This suggests that the particle size in the Subei Shoal changes significantly from winter to the summer season.

In the La Plata River Estuary, large η can be observed in the period between June and November, while small η occurs in the period between March and May (Figure 9d). In the Meghna River Estuary, η in the period between June and November shows a contrasting difference in comparison with η in the period between December and May (Figure 9e). In the period between June and November, η histogram distribution has troughs at −1.2 to −1.5, while it increases to ~ −0.5 to 0 in the period between December and May. In the Atchafalaya River Estuary (Figure 9f), η peaks at ~1.5, which is higher than those in the other regions. Specifically, the histogram of η distribution at the 1.2–1.4 bin accounts for nearly 30% of all the pixels in the period of September–November, while histograms of η distribution are widely distributed in the other three seasons.

Figure 10 shows seasonal dynamics of the PSD slope ξ in these six regions. Indeed, seasonal PSD power law slopes ξ are consistent with the seasonal changes of η in these six regions due to the ξ and η relationship as formulated in equation (7). Hangzhou Bay (Figure 10b) is featured with uniformly high ξ values in the periods of December–February (winter), March–May (spring), and September–November (autumn). In the summer season, the particle size is smaller than that in the other three seasons. In the Subei Shoal (Figure 10a), significant particle size difference can be found between the winter and summer. In the Amazon River Estuary, a smaller PSD difference is observed with peak ξ at ~3.2 for all the four seasons (Figure 10c). In the La Plata River Estuary, the highest ξ at ~4.4 occurs in the period between September–November, while the lowest ξ occurs in the period between March–May at ~3.8 (Figure 10d). In the Meghna River Estuary, there are two modes of ξ for the PSD (Figure 10e). In the periods of June–August and September–November, this region is dominated with large particles. ξ for PSD peaks at ~3.0. This can be attributed to the southwestern monsoon, which brings strong winds and rainfall to this region that can lead to river flooding and sediment resuspension. In the dry seasons of December–February and March–May, this region is featured with smaller particles with peak ξ at ~3.4. Figure 10f shows the seasonal variations of the PSD in the Atchafalaya River region. Indeed, the particle size generally is smaller for all the four seasons with ξ at ~4.4. In the period of September–November, particles are more uniformly distributed than those in the other periods.

To understand, characterize, and quantify the regional difference of the η and ξ for different regions, we further produce the changes of $nL_w(862)$, $b_{bp}(862)$, η, and ξ as a function of $nL_w(745)$. $nL_w(745)$ for all of the pixels in each region are binned at the ranges of 0–0.4, 0.4–0.8, 0.8–1.2 ... mW·cm^{-2}·μm^{-1}·sr^{-1} with a bin size of 0.4 mW·cm^{-2}·μm^{-1}·sr^{-1} in order to better characterize the relationship between $nL_w(745)$ and the other parameters. The other parameters corresponding to each $nL_w(745)$ bin in each region are also
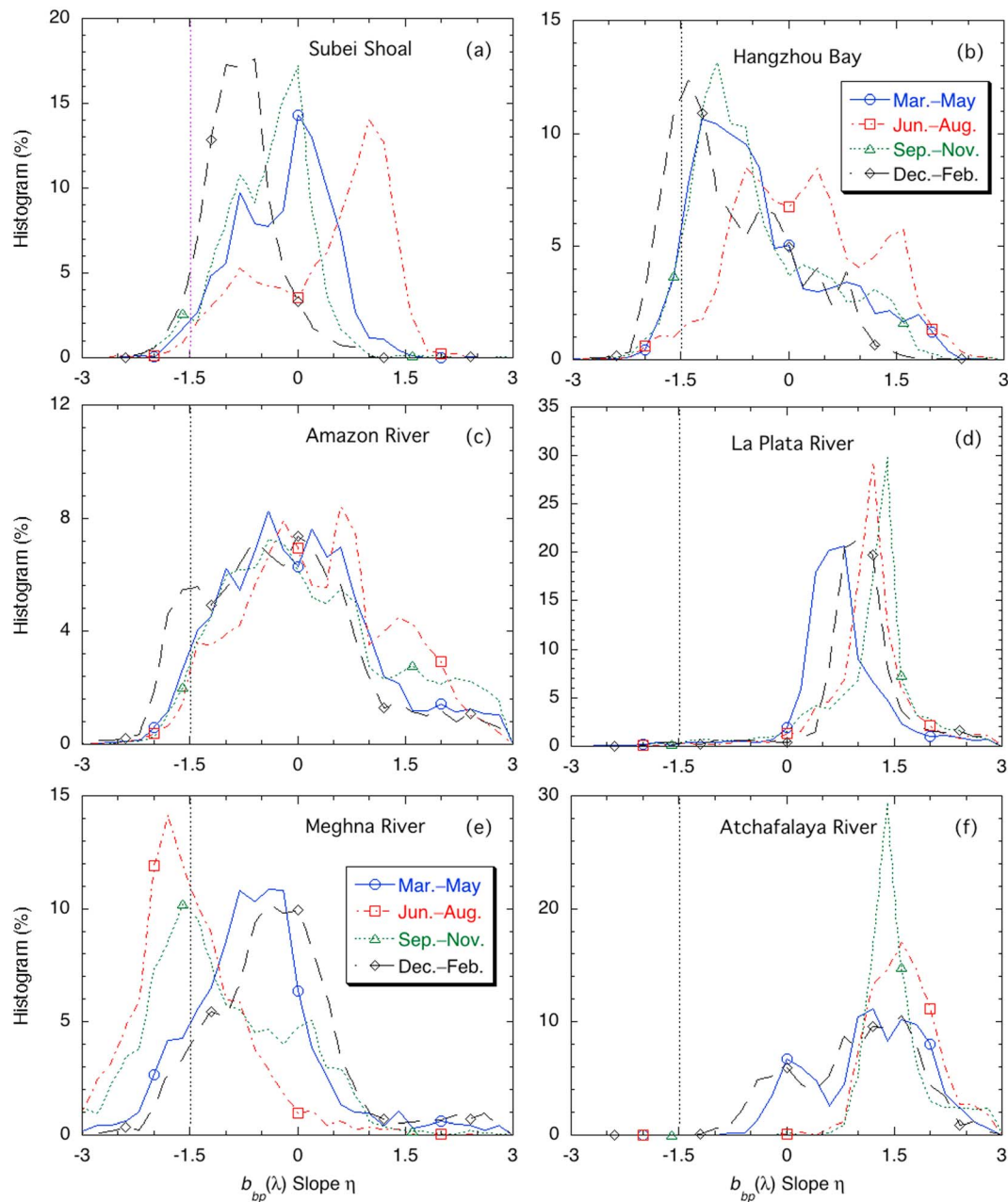
Figure 9. Histogram results of the Visible Infrared Imaging Radiometer Suite-derived seasonal $b_{bp}(\lambda)$ slope η for the six regions marked in Figure 2 for (a) Subei Shoal, (b) Hangzhou Bay, (c) Amazon River Estuary, (d) La Plata River Estuary, (e) Meghna River Estuary, and (f) Atchafalaya River Estuary. A dotted line at $\eta = -1.5$ is also marked in each plot to show the results of the extrapolated PSD slope $\eta < -1.5$.

binned. The median values of $nL_w(745)$, $nL_w(862)$, $b_{bp}(862)$, η, and ξ in each bin are computed as the representative values for the respective parameters. Note that $nL_w(745)$ in the Atchafalaya region can only reach ~2 mW·cm^{-2}·μm^{-1}·sr^{-1}.

Figure 11a shows that $nL_w(745)$ and $nL_w(862)$ have more or less similar curvatures. $nL_w(745)$ and $nL_w(862)$ from VIIRS-SNPP observations in this study are similar to $nL_w(748)$ and $nL_w(869)$ from MODIS-Aqua observations in China's east coastal region (Shi & Wang, 2014). It is noted that $nL_w(745)$ and $nL_w(862)$ are not linearly related in the entire $nL_w(745)$ range, especially for high $nL_w(745)$ values. This agrees with the assessments from several other studies (Doron et al., 2011; Shi & Wang, 2014). It is also noteworthy that the $nL_w(745)$ and $nL_w(862)$ relationship in the Meghna River Estuary is slightly off the common $nL_w(745)$
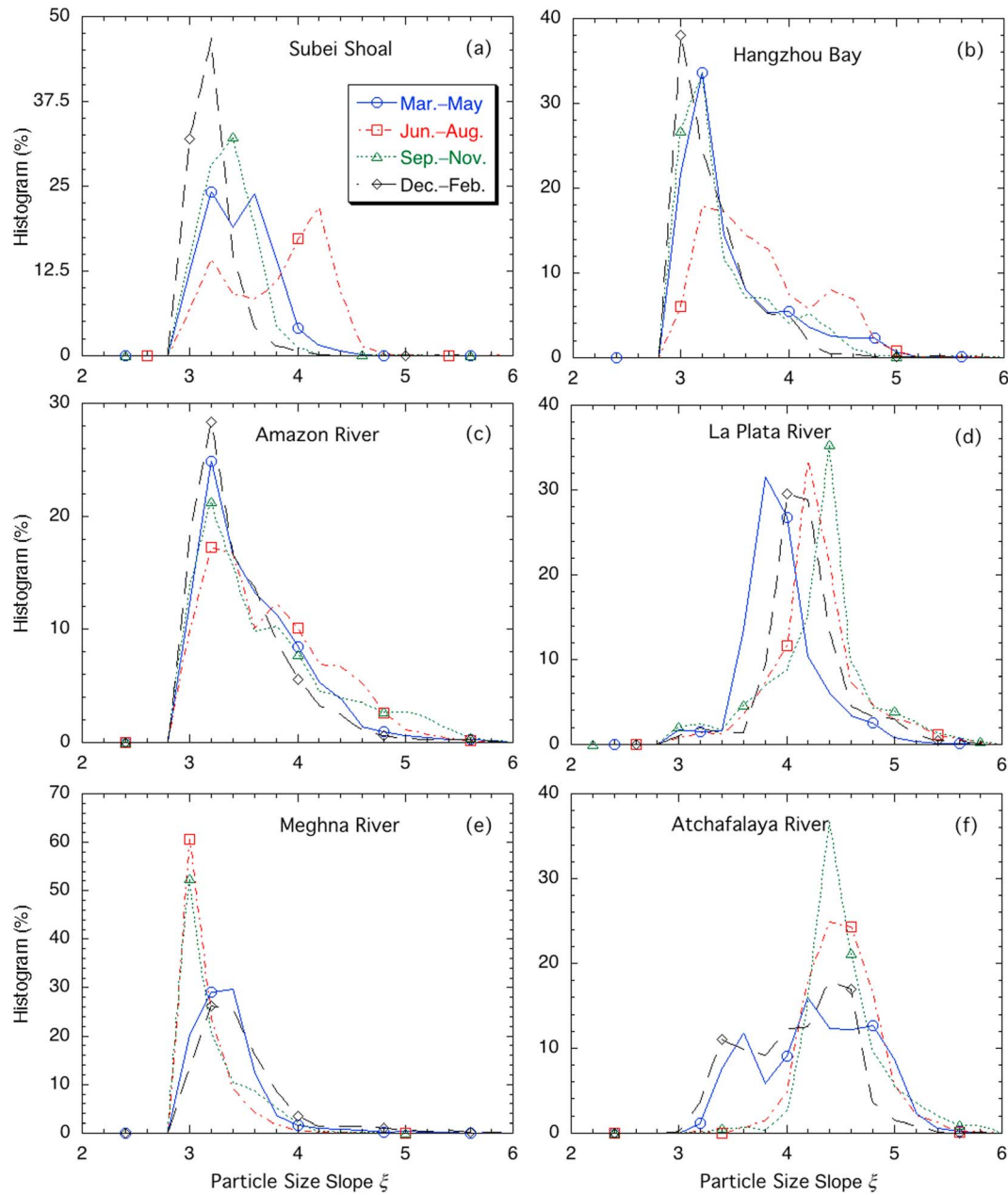
Figure 10. Histogram results of the Visible Infrared Imaging Radiometer Suite-derived particle size slope ξ for the six regions marked in Figure 2 for (a) Subei Shoal, (b) Hangzhou Bay, (c) Amazon River Estuary, (d) La Plata River Estuary, (e) Meghna River Estuary, and (f) Atchafalaya River Estuary.

and $nL_w(862)$ curve for the other regions with $nL_w(745) > 3.0$ mW·cm^{-2}·μm^{-1}·sr^{-1}. This suggests that the features of $b_{bp}(\lambda)$, η, and ξ in the Meghna River Estuary are different from those in the other regions.

Figure 11b shows variations of $b_{bp}(862)$ with changes of $nL_w(745)$ in these six regions. Note that $b_{bp}(745)$ is a function of $nL_w(745)$ as described in equations (1)–(5). Thus, the relationship between $b_{bp}(745)$ and $nL_w(745)$ is the same for all regions. Similar to the $nL_w(745)$ and $nL_w(862)$ relationship, the relationships between $b_{bp}(862)$ and $nL_w(745)$ are similar except for the one in the Meghna River. As an example, $b_{bp}(862)$ values are generally ~3.4–3.6 m^{-1}, corresponding to $nL_w(745)$ of ~3.8 mW·cm^{-2}·μm^{-1}·sr^{-1} in the Hangzhou Bay, Subei Shoal, Amazon River Estuary, and La Plata River Estuary. In comparison, $b_{bp}(862)$ values are ~4.2 m^{-1}, corresponding to $nL_w(745)$ of ~3.8 mW·cm^{-2}·μm^{-1}·sr^{-1} in the Meghna River regions. Thus, higher $b_{bp}(862)$ can lead to lower η and ξ in this region.
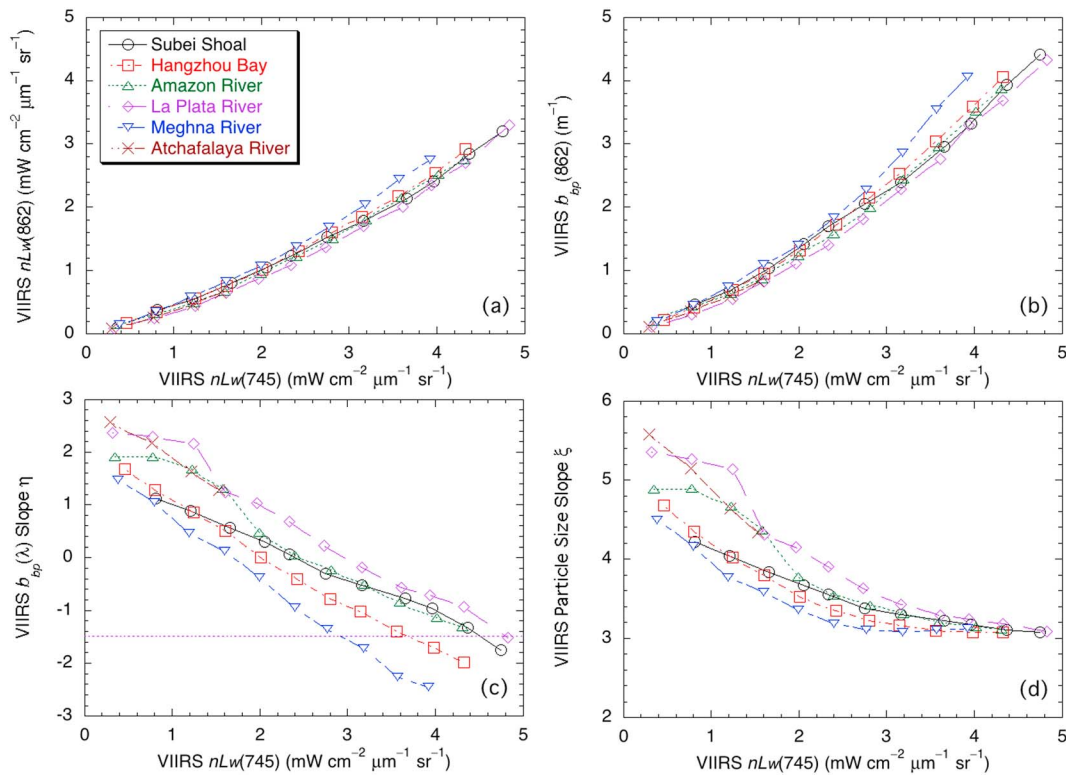
Figure 11. Visible Infrared Imaging Radiometer Suite-derived optical and particle size properties as a function of $nL_w(745)$ from the six regions marked in Figure 2 for the parameter of (a) $nL_w(862)$, (b) $b_{bp}(862)$, (c) $b_{bp}(\lambda)$ slope η, and (d) PSD slope ξ. A dotted line at $\eta = -1.5$ is also marked in plot (c) to show the results of the extrapolated PSD slope $\eta < -1.5$.

Figure 11c demonstrates the regional difference of $b_{bp}(\lambda)$ slopes. In comparison to the $nL_w(862)$ and $b_{bp}(862)$ curves (Figures 11a and 11b), notable differences in the η versus $nL_w(745)$ relationship can be found in different regions. With the same $nL_w(745)$ value, the maximum difference in η for different regions can reach up to ~1.5. As an example, η is -0.8 in the Meghna River Estuary for $nL_w(745)$ of ~2.2 mW·cm^{-2}·μm^{-1}·sr^{-1}. However, η is 0.7 in the La Plata River Estuary for similar $nL_w(745)$ values. In general, values of $b_{bp}(\lambda)$ slope η increase in the order of the Meghna River Estuary, Hangzhou Bay, Subei Shoal, Amazon River Estuary (close to Subei Shoal), and La Plata River Estuary in all these regions except for the Atchafalaya River Estuary, where $nL_w(745)$ can only reach a maximum value of ~1.6 mW·cm^{-2}·μm^{-1}·sr^{-1} and becomes difficult to evaluate. Conversely, this implies that for the same $nL_w(745)$ value the particle size decreases in the order of the Meghna River Estuary, Hangzhou Bay, Subei Shoal, Amazon River Estuary (close to Subei Shoal), and La Plata River Estuary.

In addition to the regional difference of $b_{bp}(\lambda)$ slopes η for different regions, Figure 11c also shows a monotonous relationship between $b_{bp}(\lambda)$ slope η and $nL_w(745)$. For all the regions, $b_{bp}(\lambda)$ slope η decreases with the increase of $nL_w(745)$. As an example, η is ~1.7 for $nL_w(745)$ of ~0.4 mW·cm^{-2}·μm^{-1}·sr^{-1} in Hangzhou Bay. The η becomes ~ -1.5 when $nL_w(745)$ is ~4.0 mW·cm^{-2}·μm^{-1}·sr^{-1}. This indicates that the seasonal changes of $nL_w(745)$ and $b_{bp}(\lambda)$ in these highly turbid regions (Shi & Wang, 2017) also come with the seasonal changes of the $b_{bp}(\lambda)$ slope η. In the Hangzhou Bay, $nL_w(745)$ can reach over ~3–4 mW·cm^{-2}·μm^{-1}·sr^{-1} in the winter, while it is ~1.0 mW·cm^{-2}·μm^{-1}·sr^{-1} in the summer. The corresponding $b_{bp}(\lambda)$ slope η varies between $< \sim -1.0$ in the winter and ~1.0 in the summer.

Figure 11d further illustrates the regional dependence of the PSDs for different locations. Indeed, for the scenario with $nL_w(745) < 3.0$ mW·cm^{-2}·μm^{-1}·sr^{-1}, PSD slope ξ generally increases in the sequence as described in Figure 11c. This shows that the particle size in these regions decreases in the order of the Meghna River Estuary, Hangzhou Bay, Subei Shoal, Amazon River Estuary, and La Plata River Estuary for the same

$nL_w(745)$ value. In Figure 11d, the PSD slope ξ becomes less sensitive to the change of the $nL_w(745)$ when $nL_w(745) > \sim 3.0$ mW·cm^{-2}·μm^{-1}·sr^{-1}. Indeed, at $nL_w(745)$ of ~3.0 mW·cm^{-2}·μm^{-1}·sr^{-1} and above, the particle size slope ξ is similar for all of the highly turbid regions. In Kostadinov et al. (2009), the uncertainty of the PSD slope ξ increases from ~0% to 20% with the decrease of η from +1 to −1.5. This suggests that uncertainty of ξ increases with the increase of $nL_w(745)$ in Figure 11d. It is also noted that the relationship between PSD slope ξ and $b_{bp}(\lambda)$ slope η is statistically fitted in the η range between −1.5 and 3.0. Figure 11c shows η can reach below −1.5 for some waters with $nL_w(745) > 3.0$ mW·cm^{-2}·μm^{-1}·sr^{-1} in the Meghna River Estuary or $nL_w(745) > 4.0$ mW·cm^{-2}·μm^{-1}·sr^{-1} in the Hangzhou Bay. Thus, caution should be provided and large errors may be possible for the PSD slope ξ as shown in Figure 11d in these cases.

3.4. Interannual Variability of VIIRS-Derived η and ξ in Highly Turbid Waters

The time series of η and ξ at these six regions are shown in Figure 12. For all seasons between 2012 and 2017, corresponding composites of η and ξ are produced at these six regions. The median values of seasonal η and ξ composites in the respective box as shown in Figure 2 are calculated as the representative η and ξ for that season. Remarkable seasonal cycles of η and ξ can be found in the Subei Shoal (Figure 12a) and Hangzhou Bay (Figure 12b). In the Hangzhou Bay, η ranges from ~ −1.5 to −0.8 in the boreal winter to ~0.4–0.8 in the boreal summer. Parameters η and ξ also experienced significant interannual variability. Indeed, in the summer of 2015–2016 (June–August), η only peaked at −0.2, while it reached over ~0.4 in the other years. Similar seasonal changes of η and ξ can also be found in the Subei Shoal with η (or ξ) ranging from ~ −0.8 (or 3.3) in December–February and ~0.6 (or 4.0) in the period of June–August. This represents a seasonal change of $nL_w(745)$ and $b_{bp}(\lambda)$ due to the expansion and enhancement of the sediment plumes in the Subei Shoal (Shi & Wang, 2012).

Figure 12c shows that there are no significant seasonal variations in η and ξ for the Amazon River Estuary even though η and ξ were generally lower in the period of December–February and higher in the period of June–August. It is also noted that both η and ξ (Figures 8, 9c, and 10c) are distributed in a wide range. Thus, the η and ξ in the Amazon River Estuary do not have significant peaks and troughs like the Hangzhou Bay and Subei Shoal regions as shown in Figures 12a and 12b. Figure 12d shows the interannual variations of η and ξ in the La Plata River Estuary. Indeed, both η and ξ were much higher than those in the Amazon River Estuary (Figure 12c), Subei Shoal (Figure 12a), and Hangzhou Bay (Figure 12b). The η usually changed between ~0.5 and 1.5, while ξ usually changed between ~4.0 and 4.5 in this region.

Figure 12e shows the η and ξ variations between 2012 and 2017 in the Meghna River Estuary. The Meghna River Estuary is the region with the largest particle size in the highly turbid waters of the global ocean. Specifically, η reached below −1.5 and ξ was ~3.1 in the months of June–August. For most of the time between 2012 and 2017, η was negative and ξ was below ~3.3. In addition, interannual variations of η and ξ were also significant in comparison with the other regions. Even though η normally was below ~ −1.8 in the period of June–August between 2012 and 2017, it was ~ −1.0 in the same period in 2014. In these study regions, the Atchafalaya River Estuary is featured with the smaller particle sizes. The particle size is similar to that in the La Plata River Estuary. The η varied from ~1.0 to ~1.7 and ξ ranged from ~4.0 to ~4.7 seasonally with no significant interannual variability.

4. Discussion

4.1. Driving Forcing for the Dynamics of $b_{bp}(\lambda)$, η, and ξ

In complex coastal and estuarine waters, the seasonal and interannual variation of $b_{bp}(\lambda)$ (Shi & Wang, 2017) and particle size are driven by various forces such as winds, rainfall, and river discharges. In the Amazon River Estuary, seasonal and interannual dynamics of suspended sediment at the mouth of the Amazon River is attributed to the continental forcing, that is, the Amazon River discharge and sediment discharge as well as the ocean forcing, such as winds, waves, and currents (Gensac et al., 2016). In China's east coastal region, both the in situ measurements and satellite observations show significant seasonal and interannual optical, biological, and biogeochemical variations (Shi & Wang, 2012). The major mechanisms that define the spatial patterns and cause significant variability of water properties in the Bohai Sea, Yellow Sea, and East China Sea regions are the seasonal winds and air-sea interactions driven by seasonal climate change (Shi & Wang, 2012). Other factors such as rainfall, river discharge (Shen et al., 2013), and the tides (Liu &
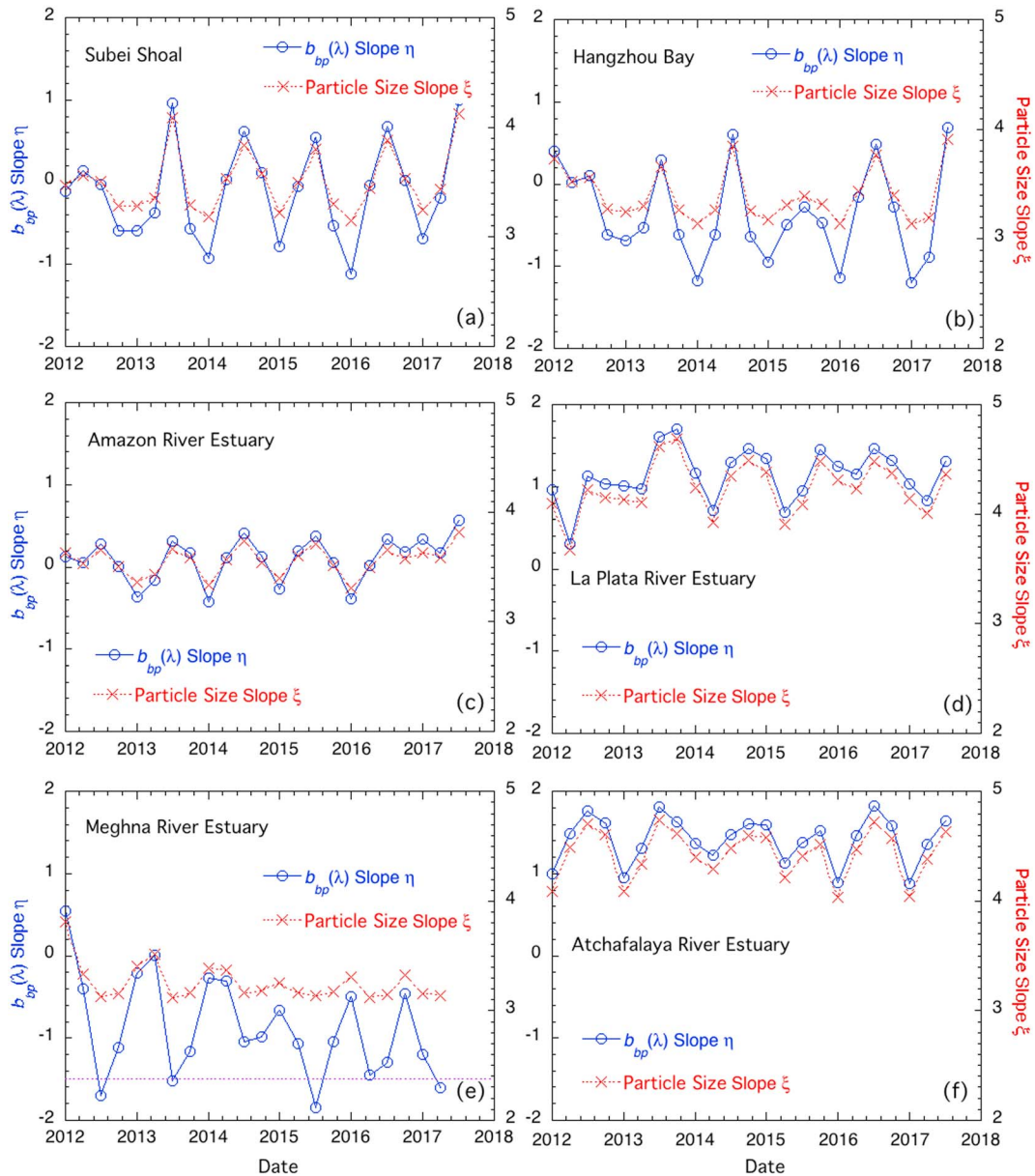
Figure 12. Visible Infrared Imaging Radiometer Suite-derived time series of η and ξ for the six regions marked in Figure 2 for (a) Subei Shoal, (b) Hangzhou Bay, (c) Amazon River Estuary, (d) La Plata River Estuary, (e) Meghna River Estuary, and (f) Atchafalaya River Estuary. A dotted line at $\eta = -1.5$ is also marked in plot (e) to show the results of the extrapolated PSD slope $\eta < -1.5$.

Wang, 2016; Shi et al., 2011) can also contribute to the variability of the particle size distribution in the coastal regions.

Using the Amazon River Estuary and Meghna River Estuary as examples, Figure 13 shows the monthly wind speed and precipitation in these two regions between 2012 and 2017. Due to lack of the river discharge data and the clear connection between the river discharge and precipitation, monthly rainfall in each region can be used as a surrogate for the seasonal and interannual dynamics of the river discharge in the region. In the Amazon River Estuary, seasonal cycles of the wind speed and rainfall are out of phase with each other, that is, strong wind speed and low precipitation occur in October–November. Results of time series in η and ξ (Figure 12c) show that the seasonal changes of η and ξ are generally in phase with the seasonal wind cycles, while peak rainfalls in the March–April season do not lead to low η and ξ that represent large size particle dominated PSD.
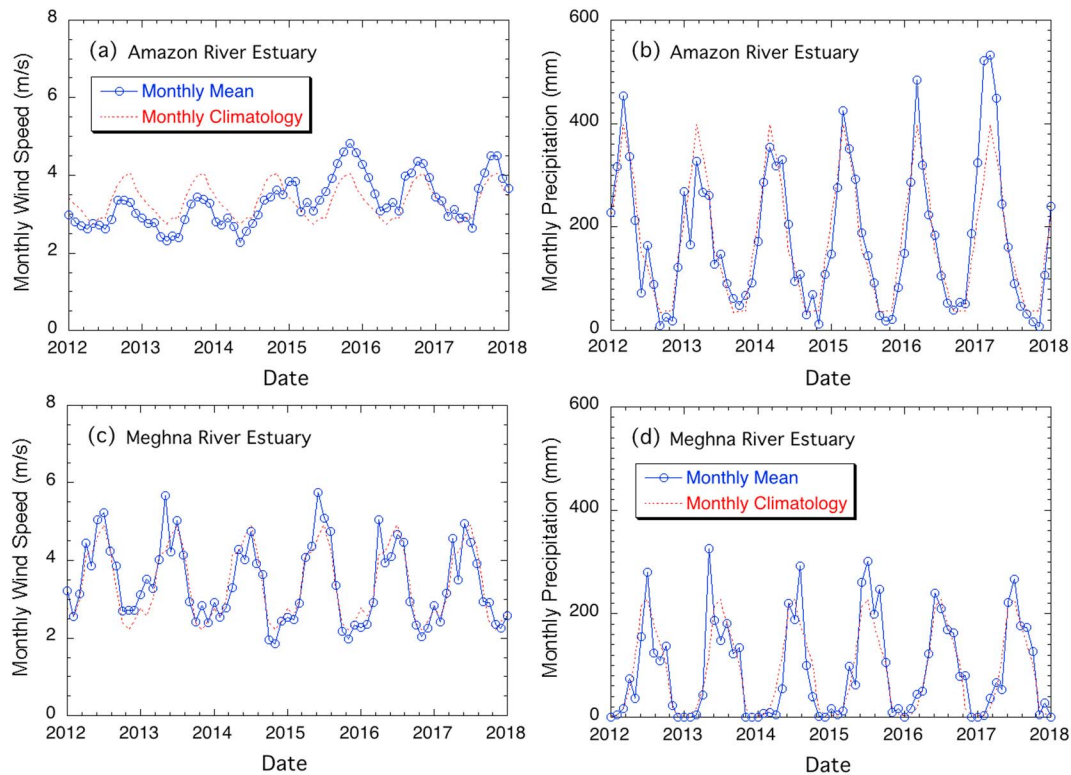
Figure 13. Time series of the monthly average wind speed and rainfall between 2012 and 2017 for (a) and (b) at the location of [0.16°S, 50.39°W] in the Amazon River Estuary, and (c) and (d) at the location of [22.28°N, 91.10°E] in the Meghna River Estuary. Seasonal climatology monthly average wind speed and rainfall are overlaid in each plot in order to compare the seasonal and interannual variability of wind speed and rainfall in each region. The locations for the monthly average wind speed and rainfall in these two regions are marked in Figures 2g and 2i.

In the Meghna River Estuary, seasonal wind speed cycles are both in phase with the seasonal rainfall cycles (Figures 13c and 13d). This reflects that the strong monsoon in the northern Indian Ocean brings in both high winds and strong rainfalls in this region. In the Meghna River Estuary, seasonal η and ξ changes (Figure 12e) are consistent with the seasonal winds and rainfalls. Specifically, anomalous η and ξ in the summer of 2015 coincided with the excessive winds in the mid-2015. In addition, enhanced seasonal variability of η and ξ in the Meghna River Estuary (Figure 12e) was also coinciding with the strong seasonal variability of the winds. The time series of wind speeds and rainfall in the Amazon River Estuary and the Meghna River Estuary show that the PSDs in these two regions are driven by the physical forcing such as the wind, rainfall, and river discharges. In fact, wind forcing is the major driver for the dynamics of the PSD in the highly turbid regions.

4.2. Uncertainties of $b_{bp}(\lambda)$, η, and ξ

Equation (4) is an important approximation that is used to derive the IOPs over highly turbid waters. It is noted that $a_d(\lambda)$ may be nonnegligible in comparison to $a_w(\lambda)$ at the NIR wavelengths in extremely turbid waters. This might lead to some uncertainties in deriving $b_{bp}(\lambda)$ with equation (4). On the other hand, $b_b(\lambda)/[a(\lambda) + b_b(\lambda)]$ is approximated to ~1.0 in extremely turbid waters when $b_b(\lambda) >> a_w(\lambda)$, and consequently $nL_w(745)$ and $nL_w(862)$ become less sensitive to the change of $b_{bp}(\lambda)$. Shi and Wang (2009) also show that MODIS-derived $nL_w(748)$ and $nL_w(859)$ can become less sensitive to the $nL_w(1240)$ at the SWIR wavelength. Indeed, these results are consistent with in situ observations (Knaeps et al., 2015; Lu et al., 2018; Nechad et al., 2010; Shen et al., 2010; Shen et al., 2010).

For VIIRS observations, equation (4) can be safely used to derive $b_{bp}(\lambda)$ when VIIRS-measured $nL_w(745)$ and $nL_w(862)$ are less than ~6 and ~4 mW·cm^{-2}·μm^{-1}·sr^{-1} (Shi & Wang, 2017), respectively. Hydrolight (Mobley et al., 1993) simulations also show that the difference of $b_b(\lambda)/[a(\lambda) + b_b(\lambda)]$ (represented as $u(\lambda)$) and $b_b(\lambda)/[a_w(\lambda) + b_b(\lambda)]$ (represented as simplified-$u(\lambda)$) is less than 0.005% for typical coastal turbid Case-2 water at

the NIR wavelengths (Shi & Wang, 2017). In this study, $nL_w(745)$ in these turbid waters are less than ~5 mW·cm^{-2}·μm^{-1}·sr^{-1} (Figure 11). This suggests that the absorption can be largely negligible for the NIR wavelengths, which are used in equation (4), even though the absorption indeed is not negligible for the visible bands (especially for the short blue band at 410 nm).

In this study, η as shown in equation (5) is determined from the $b_{bp}(\lambda)$ at the NIR wavelengths. However, η values in equation (5) are statistically fit with $b_{bp}(\lambda)$ at the wavelengths of 490, 510, and 555 nm in Kostadinov et al. (2009). The physics of the same spectral relationship of $b_{bp}(\lambda)$ at the NIR wavelengths and at the visible is based on the same Mie scattering theory for both marine particle and atmospheric aerosols. Thus, equation (5) is a reasonably accurate approximation to formulate the spectral dependency of $b_{bp}(\lambda)$ (Gordon & Morel, 1983; IOCCG, 2006), and η values for the visible bands and NIR bands are consistent. Field experiments in the Elbe and Gironde River Estuaries in Europe show that the particle backscattering coefficient $b_{bp}(\lambda)$ closely matches the power law relationship at the NIR wavelengths, and the power law slope η is generally consistent with the $b_p(\lambda)$ power law slope in the visible (Doxaran et al., 2007). Stramski et al. (2007) also showed that $b_p(\lambda)$ spectra are wavelength dependent and follow the power law of the wavelength (~$\lambda^{-\eta}$).

On the other hand, Kostadinov et al. (2009) show that the power law fit for $b_{bp}(\lambda)$ is poor in coastal waters and attribute this to the absorption effect (Loisel et al., 2006). Considering that the particle absorption effects are only significant at the VIIRS 410- and 443-nm bands, η values derived from the NIR bands are reasonably accurate for the wavelength range between the green and NIR wavelengths. Thus, the Kostadinov et al. (2009) formula can be used to compute the particle size slope. Shi and Wang (2014, 2017) showed that $b_{bp}(\lambda)$ in the entire spectrum can be derived using the known $b_{bp}(\lambda)$ at the two NIR bands with good accuracy. These evidently show that the power law slope η derived with the input of $b_{bp}(\lambda)$ at the two NIR bands can be used to quantify the spectral relationships for $b_{bp}(\lambda)$ at different VIIRS bands, even though the possible biases of $b_{bp}(\lambda)$ might exist for the deep blue and blue bands.

The uncertainty in the PSD slope ξ is higher in these highly turbid regions than that in the open ocean (Kostadinov et al., 2009). From Kostadinov et al. (2009), the uncertainty of PSD slope ξ from the Mie scattering simulations is ~0.20 for η ~ −1.3 to −1.5 (ξ ~3.0). More uncertainties are expected for the PSD slope ξ for $\eta <$ ~ −1.5 since equation (7) is derived for the η range above −1.5. The uncertainty of PSD slope ξ decreases with increase of η and ξ. It reaches ~0.15 for η ~ 0 (or ξ ~ 3.53). This suggests that uncertainty of the PDF slope ξ is generally one order of magnitude smaller than the PSD slope ξ and its variability. The uncertainty for ξ is expected to be ~0.15–0.20 in China's east coastal region and Meghna River Estuary and even lower ξ uncertainty in the La Plata River Estuary and Atchafalaya River Estuary. Note that these uncertainties are only the uncertainties from the Kostadinov et al. (2009) formulation. They do not include the uncertainties of the propagating errors in the power law slope η calculation from the satellite $nL_w(\lambda)$ retrievals.

Even though it is a challenging work to accurately evaluate the propagation of the errors in the satellite ocean color data processing from the VIIRS SDR data to the $b_{bp}(\lambda)$ power law slope η and PSD power law slope ξ, it would be helpful to provide a first-order estimation of the uncertainties from mathematical equations in each level of the parameters when computing η and ξ. To estimate the propagation of the error, we insert the $nL_w(\lambda)$ uncertainties in equation (1) and then compute the errors in each step numerically following equations (1)–(7). Assuming the uncertainty for $nL_w(745)$ is 5% which is similar to the uncertainties for the visible bands (McClain, 2009), it can lead to 3% of uncertainty in $b_{bp}(745)$. Uncertainty of 3% in $b_{bp}(745)$ consequently can cause ~20% of the η uncertainty for water with η = 1.0. This will further lead to ~15% of uncertainty in PSD slope ξ. Note that these uncertainty propagations are the first-order estimations from atmospheric correction to the PSD slope ξ in the VIIRS ocean color data processing. The consequent uncertainty of PSD slope ξ in the data processing is the additional uncertainty over the uncertainty of the PSD slope ξ algorithm in the VIIRS-derived PSD slope product.

Kostadinov et al. (2009) have shown that satellite-based retrievals of PSD slope ξ agree reasonably well with limited field observations. In this study, VIIRS PSD slope ξ retrievals in the coastal and estuarine waters qualitatively agree with the in situ particle size observations (Buonassissi & Dierssen, 2010; Qiu et al., 2016; Xi et al., 2014). Note that these in situ data were measured with Laser In-situ Scattering and Transmissometry

particle analyzer (Sequoia, Inc), which can analyze the particle size for the particle size spectra between 1 and 100 μm instead of the small-size range of the particle size like the Coulter counter. The particle size slope ξ trends lower with increasing $nL_w(\lambda)$ in all the highly turbid regions. Using $nL_w(\lambda)$ at the NIR wavelength as a surrogate for the total suspended matter (TSM) concentration, there is an implication that particle size in the water column is larger in the high TSM waters, and vice versa, that is, particle size generally decreases from the inshore to offshore regions. This trend of the particle size as illustrated from this study is supported by various oceanographic in situ measurements (Kitchen et al., 1982; Park et al., 2001; Xi et al., 2014) and satellite observations (Kostadinov et al., 2009; Loisel et al., 2006). In all, these qualitative comparisons between VIIRS retrievals and in situ particle size measurements in coastal turbid waters further suggest that PSD can be characterized with equation (7) in global highly turbid waters even though various uncertainties indeed exist.

Equation (7) converts η to ξ and is derived from Mie scattering simulations (Mie, 1908), where the scatters are assumed to be homogenous spherical particles. However, the spherical particle assumption is generally not true for particles in ocean or over highly turbid coastal and inland waters (Clavano et al., 2007; Gordon, 2011; Jonasz, 1987b; Quirantes & Bernard, 2004). Thus, there might be some uncertainties and errors with the satellite-derived PSD slope ξ using equation (7). In fact, the backscattering of spheroids is likely to be ~10% and even larger than the backscattering of equal-volume spherical particles, depending on the PSD slope ξ, particle refractive index, and the particle aspect ratio (Clavano et al., 2007). Large particles are expected to deviate more from sphericity (Jonasz, 1987a, 1987b); thus, higher uncertainty in the equation is more likely in the coastal waters since large particles are dominant in coastal and inland waters.

Gordon (2011) also showed that an equal-volume spherical particle assumption can lead to underestimation (overestimation) of the backscattering for a special example of the cylinder-like particle for low (high) refractive index particles. Thus, this suggests that uncertainty from the Mie scattering simulations for nonspherical particles is also strongly related to the variability of the particle refractive index. On the other hand, $b_{bp}(\lambda)$ slope η in equation (6) is computed from equation (5) as proportional to the logarithmic value of $b_{bp}(\lambda)/b_{bp}(\lambda_0)$. Correspondingly, the possible biases of η as well as ξ is largely reduced because they cancelled out each other in the ratio of $b_{bp}(\lambda)/b_{bp}(\lambda_0)$. In all, equation (7) from the Mie scattering can indeed provide a reasonable first-order estimation of the PSD slope ξ even with possible uncertainty in equation (7) due to the effect of the particle nonsphericity on the backscattering simulation using the Mie scattering theory.

4.3. Implications for the IOP Properties

Figure 11 has some important implications about the IOP properties. The monotonous quasi-linear relationships between $nL_w(745)$ and $b_{bp}(\lambda)$ in Figure 11b show that the particle concentrations exert the first order control over the $b_{bp}(\lambda)$ magnitude, while the nonlinearity between $nL_w(745)$ and $b_{bp}(\lambda)$ reflects the second order controls due to the changes of PSD distributions with the $nL_w(745)$ in each same region as shown in Figure 11d. It is noted that the difference of $b_{bp}(\lambda)$ for the same $nL_w(745)$ in the different regions may also be due to the different particle compositions and particle shapes in addition to the PSD differences.

The number of the particles per volume of the seawater $N(D)$, that is, particle number density, is determined by both ξ and the reference number of particles N_0 at the reference diameter D_0. The ξ can provide the profile of the PSDs in the water column. In this study, only the power law slope ξ is produced with the given empirical relationship between ξ and η in Kostadinov et al. (2009) from Mie simulations. The reference number of particles N_0 is not generated in this study due to the relatively larger uncertainty of the N_0 (Kostadinov et al., 2009). For $b_{bp}(\lambda)$ slope $\eta = -1.5$, $\log_{10}(b_{bp}(440)/N_0)$ is -18.899 with the uncertainty of 0.422. This implies that the upper bound of N_0 can be a couple of times higher than the lower bound of N_0 in terms of the N_0 range due to its uncertainty. In comparison to the uncertainty of $\log_{10}(b_{bp}(440)/N_0)$, Kostadinov et al. (2009) show that power law slope ξ has less uncertainty in the range of $\eta < 0$. This suggests that the possible errors for the refraction index in the Mie simulations in Kostadinov et al. (2009) will have bigger effects on the N_0 retrieval than on the PSD slope ξ.

The results from Kostadinov et al. (2009) suggest that reference N_0 at 2 μm is a function of both ξ and $b_{bp}(\lambda)$. N_0 is nonlinearly proportional to the value of $b_{bp}(\lambda)$, that is, N_0 increases correspondingly with the increase of $b_{bp}(\lambda)$ when the PSD slope ξ is the same. Thus, this implies that $b_{bp}(\lambda)$ maps as shown in Figure 2 and Shi

and Wang (2017) are more or less representative of the abundance of the particles at the reference particle size D_0.

5. Conclusion

In this study, we developed a NIR-based algorithm for both $b_{bp}(\lambda)$ power law slope η and particle size slope ξ for turbid coastal and inland waters. Using the NIR-based η and ξ algorithms, we have characterized and quantified η and ξ in the major turbid waters of the global ocean with the VIIRS-SNPP observations between 2012 and 2017. Seasonal and interannual variations of η and ξ in China's east coastal region, the Amazon River Estuary, the La Plata River Estuary, the Meghna River Estuary, and the Atchafalaya River Estuary are analyzed. η can reach below ~ -1.0 and ξ can reach below ~ 3.5 in some highly turbid regions. In China's east coastal region, η and ξ data show significant seasonal variations in the Subei Shoal and Hangzhou Bay. In particular, VIIRS-derived η and ξ data in the winter season are remarkably lower than those in the summer season. No significant seasonal variations of η and ξ are found in the Amazon River Estuary even though it is identified as the most turbid region in the global ocean in terms of the $nL_w(\lambda)$ and $b_{bp}(\lambda)$ magnitudes at the NIR wavelengths (Shi & Wang, 2010, 2017). The particle size spatial distributions, regional variation, and the temporal variability as illustrated in this study help us to better characterize the dynamics of suspended particles, monitor coastal ecosystem, and understand the coastal and estuarine physical and biogeochemical dynamics, as well as to further improve coastal and estuarine models.

References

Ahn, J. H. (2012). Size distribution and settling velocities of suspended particles in a tidal embayment. *Water Research*, *46*(10), 3219–3228. https://doi.org/10.1016/j.watres.2012.03.038

Arnone, R. A., Martinolich, P. , Gould, R. W., Sydor, M., & Stumpf, R. P. (1998). Coastal optical properties using SeaWiFS, Presented at Ocean Optics XIV, Kailua-Kona, HI, November 10-13, 1998.

Babin, M., Morel, A., Fournier-Sicre, V., Fell, F., & Stramski, D. (2003). Light scattering properties of marine particles in coastal and open ocean waters as related to the particle mass concentration. *Limnology and Oceanography*, *48*(2), 843–859. https://doi.org/10.4319/lo.2003.48.2.0843

Baker, E. T., & Lavelle, J. W. (1984). The effect of particle-size on the light attenuation coefficient of natural suspensions. *Journal of Geophysical Research*, *89*(C5), 8197–8203. https://doi.org/10.1029/JC089iC05p08197

Boss, E., Slade, W., & Hill, P. (2009). Effect of particulate aggregation in aquatic environments on the beam attenuation and its utility as a proxy for particulate mass. *Optics Express*, *17*(11), 9408–9420. https://doi.org/10.1364/OE.17.009408

Boss, E., Twardowski, M. S., & Herring, S. (2001). Shape of the particulate beam attenuation spectrum and its inversion to obtain the shape of the particulate size distribution. *Applied Optics*, *40*(27), 4885–4893. https://doi.org/10.1364/AO.40.004885

Bowers, D. G., & Binding, C. E. (2006). The optical properties of mineral suspended particles: A review and synthesis. *Estuarine Coastal and Shelf Science*, *67*(1-2), 219–230. https://doi.org/10.1016/j.ecss.2005.11.010

Bowers, D. G., Binding, C. E., & Ellis, K. M. (2007). Satellite remote sensing of the geographical distribution of suspended particle size in an energetic shelf sea. *Estuarine Coastal and Shelf Science*, *73*(3-4), 457–466. https://doi.org/10.1016/j.ecss.2007.02.005

Buonassissi, C. J., & Dierssen, H. M. (2010). A regional comparison of particle size distributions and the power law approximation in oceanic and estuarine surface waters. *Journal of Geophysical Research*, *115*(C10). https://doi.org/10.1029/2010JC006256

Ceronio, A. D., & Haarhoff, J. (2005). An improvement on the power law for the description of particle size distributions in potable water treatment. *Water Research*, *39*(2-3), 305–313. https://doi.org/10.1016/j.watres.2004.09.023

Clark, D. K., Gordon, H. R., Voss, K. J., Ge, Y., Broenkow, W., & Trees, C. (1997). Validation of atmospheric correction over the oceans. *Journal of Geophysical Research*, *102*(D14), 17209–17217. https://doi.org/10.1029/96JD03345

Clavano, W. R., Boss, E., & Karp-Boss, L. (2007). Inherent optical properties of non-spherical marine-like particles—From theory to observation. *Oceanography and Marine Biology*, *45*(45), 1–38.

Doron, M., Belanger, S., Doxaran, D., & Babin, M. (2011). Spectral variations in the near-infrared ocean reflectance. *Remote Sensing of Environment*, *115*(7), 1617–1631. https://doi.org/10.1016/j.rse.2011.01.015

Doxaran, D., Babin, M., & Leymarie, E. (2007). Near-infrared light scattering by particles in coastal waters. *Optics Express*, *15*(20), 12,834–12,849. https://doi.org/10.1364/OE.15.012834

Doxaran, D., Froidefond, J. M., Lavender, S., & Castaing, P. (2002). Spectral signature of highly turbid waters—Application with SPOT data to quantify suspended particulate matter concentrations. *Remote Sensing of Environment*, *81*(1), 149–161. https://doi.org/10.1016/S0034-4257(01)00341-8

Dyer, K. R., Christie, M. C., Feates, N., Fennessy, M. J., Pejrup, M., & van der Lee, W. (2000). An investigation into processes influencing the morphodynamics of an intertidal mudflat, the Dollard estuary, the Netherlands: I. Hydrodynamics and suspended sediment. *Estuarine Coastal and Shelf Science*, *50*(5), 607–625. https://doi.org/10.1006/ecss.1999.0596

Eisma, D., Schuhmacher, T., Boekel, H., Vanheerwaarden, J., Franken, H., Laan, M., et al. (1990). A camera and image-analysis system for in situ observation of flocs in natural-waters. *Netherlands Journal of Sea Research*, *27*(1), 43–56. https://doi.org/10.1016/0077-7579(90)90033-D

Ellis, K. M., Bowers, D. G., & Jones, S. E. (2004). A study of the temporal variability in particle size in a high-energy regime. *Estuarine Coastal and Shelf Science*, *61*(2), 311–315. https://doi.org/10.1016/j.ecss.2004.06.001

Falkowski, P. G., Barber, R. T., & Smetacek, V. (1998). Biogeochemical controls and feedbacks on ocean primary production. *Science*, *281*(5374), 200–206. https://doi.org/10.1126/science.281.5374.200

Gensac, E., Martinez, J. M., Vantrepotte, V., & Anthony, E. J. (2016). Seasonal and inter-annual dynamics of suspended sediment at the mouth of the Amazon river: The role of continental and oceanic forcing, and implications for coastal geomorphology and mud bank formation. *Continental Shelf Research*, *118*, 49–62. https://doi.org/10.1016/j.csr.2016.02.009

Goldberg, M. D., Kilcoyne, H., Cikanek, H., & Mehta, A. (2013). Joint Polar Satellite System: The United States next generation civilian polar-orbiting environmental satellite system. *Journal of Geophysical Research: Atmospheres*, *118*, 13,463–13,475. https://doi.org/10.1002/2013JD020389

Gordon, H. R. (2011). Light scattering and absorption by randomly-oriented cylinders: Dependence on aspect ratio for refractive indices applicable for marine particles. *Optics Express*, *19*(5), 4673–4691. https://doi.org/10.1364/OE.19.004673

Gordon, H. R., Brown, O. B., Evans, R. H., Brown, J. W., Smith, R. C., Baker, K. S., & Clark, D. K. (1988). A semianalytic radiance model of ocean color. *Journal of Geophysical Research*, *93*(D9), 10,909–10,924. https://doi.org/10.1029/JD093iD09p10909

Gordon, H. R., & Wang, M. (1994). Retrieval of water-leaving radiance and aerosol optical thickness over the oceans with SeaWiFS: A preliminary algorithm. *Applied Optics*, *33*, 443–452. https://doi.org/10.1364/ao.33.000443

Gordon, H. R., & Morel, A. (1983). *Remote assessment of ocean color for interpretation of satellite visible imagery: A review*. New York: Spring-verlag. https://doi.org/10.1029/LN004

IOCCG (2006). Remote sensing of inherent optical properties: Fundamentals, tests of algorithms, and applications. In Z. Lee (Ed.), *Reports of the International Ocean-Colour Coordinating Group* (No. 5, p. 125). Dartmouth, Canada: IOCCG.

Jonasz, M. (1987a). Nonspherical sediment particles—Comparison of size and volume distributions obtained with an optical and a resistive particle counter. *Marine Geology*, *78*(1-2), 137–142. https://doi.org/10.1016/0025-3227(87)90072-7

Jonasz, M. (1987b). Nonsphericity of suspended marine particles and its influence on light-scattering. *Limnology and Oceanography*, *32*(5), 1059–1065. https://doi.org/10.4319/lo.1987.32.5.1059

Junge, C. E. (1963). *Air chemistry and radioactivity*. New York: Academic.

Kitchen, J. C., Menzies, D., Pak, H., & Zaneveld, J. R. V. (1975). Particle-size distributions in a region of coastal upwelling analyzed by characteristic vectors. *Limnology and Oceanography*, *20*(5), 775–783. https://doi.org/10.4319/lo.1975.20.5.0775

Kitchen, J. C., Zaneveld, J. R. V., & Pak, H. (1982). Effect of particle-size distribution and chlorophyll content on beam attenuation spectra. *Applied Optics*, *21*(21), 3913–3918. https://doi.org/10.1364/AO.21.003913

Knaeps, E., Ruddick, K. G., Doxaran, D., Dogliotti, A. I., Nechad, B., Raymaekers, D., & Sterckx, S. (2015). A SWIR based algorithm to retrieve total suspended matter in extremely turbid waters. *Remote Sensing of Environment*, *168*, 66–79. https://doi.org/10.1016/j.rse.2015.06.022

Kostadinov, T. S., Siegel, D. A., & Maritorena, S. (2009). Retrieval of the particle size distribution from satellite ocean color observations. *Journal of Geophysical Research*, *114, C09015*. https://doi.org/10.1029/2009JC005303

Le Quere, C., Harrison, S. P., Prentice, I. C., Buitenhuis, E. T., Aumont, O., Bopp, L., et al. (2005). Ecosystem dynamics based on plankton functional types for global ocean biogeochemistry models. *Global Change Biology*, *11*(11), 2016–2040.

Lee, Z. P., Carder, K. L., Mobley, C. D., Steward, R. G., & Patch, J. S. (1999). Hyperspectral remote sensing for shallow waters: 2. Deriving bottom depths and water properties by optimization. *Applied Optics*, *38*(18), 3831–3843. https://doi.org/10.1364/AO.38.003831

Liu, X. M., & Wang, M. H. (2016). Analysis of ocean diurnal variations from the Korean Geostationary Ocean Color Imager measurements using the DINEOF method. *Estuarine Coastal and Shelf Science*, *180*, 230–241. https://doi.org/10.1016/j.ecss.2016.07.006

Loisel, H., Nicolas, J. M., Sciandra, A., Stramski, D., & Poteau, A. (2006). Spectral dependency of optical backscattering by marine particles from satellite remote sensing of the global ocean. *Journal of Geophysical Research*, *111*(C9). https://doi.org/10.1029/2005JC003367

Lu, Y. F., Doxaran, D., Ruddick, K., Shen, F., Gentili, B., Yan, L. W., & Huang, H. J. (2018). Saturation of water reflectance in extremely turbid media based on field measurements, satellite data and bio-optical modelling. *Optics Express*, *26*(8), 10,435–10,451. https://doi.org/10.1364/OE.26.010435

Maranon, E. (2015). Cell size as a key determinant of phytoplankton metabolism and community structure. *Annual Review of Marine Science*, *7*(1), 241–264. https://doi.org/10.1146/annurev-marine-010814-015955

Mccave, I. N. (1975). Vertical flux of particles in ocean. *Deep-Sea Research*, *22*(7), 491–502.

McClain, C. R. (2009). A decade of satellite ocean color observations. *Annual Review of Marine Science*, *1*(1), 19–42. https://doi.org/10.1146/annurev.marine.010908.163650

Mie, G. (1908). Beiträge zur Optik trüber Medien, speziell kolloidaler Metallösungen. *Annalen der Physik*, *330*(3), 377–445. https://doi.org/10.1002/andp.19083300302

Mobley, C. D., Gentili, B., Gordon, H. R., Jin, Z. H., Kattawar, G. W., Morel, A., et al. (1993). Comparison of numerical-models for computing underwater light fields. *Appl Optics*, *32*(36), 7484–7504. https://doi.org/10.1364/AO.32.007484

Mobley, C. D., Sundman, L. K., & Boss, E. (2002). Phase function effects on oceanic light fields. *Applied Optics*, *41*(6), 1035–1050. https://doi.org/10.1364/AO.41.001035

Morel, A. (1973). Diffusion de la lumière par les eaux de mer. In *Résultats expérimentaux et approche théorique*, (pp. 1–76). London.

Nechad, B., Ruddick, K. G., & Park, Y. (2010). Calibration and validation of a generic multisensor algorithm for mapping of total suspended matter in turbid waters. *Remote Sensing of Environment*, *114*(4), 854–866. https://doi.org/10.1016/j.rse.2009.11.022

Pannard, A., Bormans, M., Lefebvre, S., Claquin, P., & Lagadeuc, Y. (2007). Phytoplankton size distribution and community structure: Influence of nutrient input and sedimentary loss. *Journal of Plankton Research*, *29*(7), 583–598. https://doi.org/10.1093/plankt/fbm040

Park, Y. A., Choi, J. Y., & Gao, S. (2001). Spatial variation of suspended particulate matter in the Yellow Sea. *Geo-Marine Letters*, *20*(4), 196–200.

Qiu, Z. F., Sun, D. Y., Hu, C. M., Wang, S. Q., Zheng, L. F., Huan, Y., & Peng, T. (2016). Variability of particle size distributions in the Bohai Sea and the Yellow Sea. *Remote Sensing*, *8*(11). https://doi.org/10.3390/rs8110949

Quirantes, A., & Bernard, S. (2004). Light scattering by marine algae: Two-layer spherical and nonspherical models. *Journal of Quantitative Spectroscopy & Radiative Transfer*, *89*(1-4), 311–321. https://doi.org/10.1016/j.jqsrt.2004.05.031

Renosh, P. R., Schmitt, F. G., & Loisel, H. (2015). Intermittent particle dynamics in marine coastal waters. *Nonlinear Processes in Geophysics*, *22*(5), 633–643. https://doi.org/10.5194/npg-22-633-2015

Renosh, P. R., Schmitt, F. G., Loisel, H., Sentchev, A., & Meriaux, X. (2014). High frequency variability of particle size distribution and its dependency on turbulence over the sea bottom during re-suspension processes. *Continental Shelf Research*, *77*, 51–60. https://doi.org/10.1016/j.csr.2014.01.024

Risovic, D. (1993). Two-component model of sea particle-size distribution. *Deep-Sea Research Part I-Oceanographic Research Papers*, *40*(7), 1459–1473. https://doi.org/10.1016/0967-0637(93)90123-K

Ruddick, K. G., De Cauwer, V., Park, Y. J., & Moore, G. (2006). Seaborne measurements of near infrared water-leaving reflectance: The similarity spectrum for turbid waters. *Limnology and Oceanography*, *51*(2), 1167–1179. https://doi.org/10.4319/lo.2006.51.2.1167

Sheldon, R. W., Sutcliffe, W. H., & Prakash, A. (1972). Size distribution of particles in ocean. *Limnology and Oceanography*, *17*(3), 327–340. https://doi.org/10.4319/lo.1972.17.3.0327

Shen, F., Salama, M. S., Zhou, Y. X., Li, J. F., Su, Z. B., & Kuang, D. B. (2010). Remote-sensing reflectance characteristics of highly turbid estuarine waters—A comparative experiment of the Yangtze River and the Yellow River. *International Journal of Remote Sensing*, *31*(10), 2639–2654. https://doi.org/10.1080/01431160903085610

Shen, F., Verhoef, W., Zhou, Y. X., Salama, M. S., & Liu, X. L. (2010). Satellite estimates of wide-range suspended sediment concentrations in Changjiang (Yangtze) Estuary using MERIS data. *Estuaries and Coasts*, *33*(6), 1420–1429. https://doi.org/10.1007/s12237-010-9313-2

Shen, F., Zhou, Y. X., Li, J. F., He, Q., & Verhoef, W. (2013). Remotely sensed variability of the suspended sediment concentration and its response to decreased river discharge in the Yangtze estuary and adjacent coast. *Continental Shelf Research*, *69*, 52–61. https://doi.org/10.1016/j.csr.2013.09.002

Shi, W., & Wang, M. (2009). An assessment of the black ocean pixel assumption for MODIS SWIR bands. *Remote Sensing of Environment*, *113*(8), 1587–1597. https://doi.org/10.1016/j.rse.2009.03.011

Shi, W., & Wang, M. (2010). Characterization of global ocean turbidity from Moderate Resolution Imaging Spectroradiometer ocean color observations. *Journal of Geophysical Research-Oceans*, *115*(C11). https://doi.org/10.1029/2010JC006160

Shi, W., & Wang, M. (2012). Satellite views of the Bohai Sea, Yellow Sea, and East China Sea. *Progress in Oceanography*, *104*, 30–45. https://doi.org/10.1016/j.pocean.2012.05.001

Shi, W., & Wang, M. (2014). Ocean reflectance spectra at the red, near-infrared, and shortwave infrared from highly turbid waters: A study in the Bohai Sea, Yellow Sea, and East China Sea. *Limnology and Oceanography*, *59*(2), 427–444. https://doi.org/10.4319/lo.2014.59.2.0427

Shi, W., & Wang, M. (2017). Characterization of particle backscattering of global highly turbid waters from VIIRS ocean color observations. *Journal of Geophysical Research: Oceans*, *122*, 9255–9275. https://doi.org/10.1002/2017JC013191

Shi, W., Wang, M., & Jiang, L. (2011). Spring-neap tidal effects on satellite ocean color observations in the Bohai Sea, Yellow Sea, and East China Sea. *Journal of Geophysical Research*, *116*(C12). https://doi.org/10.1029/2011JC007234

Slade, W. H., & Boss, E. (2015). Spectral attenuation and backscattering as indicators of average particle size. *Applied Optics*, *54*(24), 7264–7277. https://doi.org/10.1364/AO.54.007264

Stramski, D., Babin, M., & Wozniak, S. B. (2007). Variations in the optical properties of terrigenous mineral-rich particulate matter suspended in seawater. *Limnology and Oceanography*, *52*(6), 2418–2433. https://doi.org/10.4319/lo.2007.52.6.2418

Stumpf, R. P., Arnone, R. A., Gould, R. W., Martinolich, P. M., & Ransibrahmanakul, V. (2003), *A partially coupled ocean-atmosphere model for retrieval of water-leaving radiance from SeaWiFS in coastal waters, SeaWiFS Postlaunch Technical Report Series*, 51-59 pp, NASA Goddard Space Flight Center, Greenbelt, Maryland.

Twardowski, M. S., Boss, E., Macdonald, J. B., Pegau, W. S., Barnard, A. H., & Zaneveld, J. R. V. (2001). A model for estimating bulk refractive index from the optical backscattering ratio and the implications for understanding particle composition in case I and case II waters. *Journal of Geophysical Research*, *106*(C7), 14,129–14,142. https://doi.org/10.1029/2000JC000404

Ulloa, O., Sathyendranath, S., & Platt, T. (1994). Effect of the particle-size distribution on the backscattering ratio in seawater. *Applied Optics*, *33*(30), 7070–7077. https://doi.org/10.1364/AO.33.007070

Wang, M. (1999). A sensitivity study of the SeaWiFS atmospheric correction algorithm: Effects of spectral band variations. *Remote Sensing of Environment*, *67*(3), 348–359. https://doi.org/10.1016/S0034-4257(98)00095-9

Wang, M. (2007). Remote sensing of the ocean contributions from ultraviolet to near-infrared using the shortwave infrared bands: Simulations. *Applied Optics*, *46*(9), 1535–1547. https://doi.org/10.1364/AO.46.001535

Wang, M., & Franz, B. A. (2000). Comparing the ocean color measurements between MOS and SeaWiFS: A vicarious intercalibration approach for MOS. *IEEE Transactions on Geoscience and Remote Sensing*, *38*(1), 184–197. https://doi.org/10.1109/36.823911

Wang, M., & Jiang, L. D. (2018). VIIRS-derived ocean color product using the imaging bands. *Remote Sensing of Environment*, *206*, 275–286. https://doi.org/10.1016/j.rse.2017.12.042

Wang, M., Liu, X., Tan, L., Jiang, L., Son, S., Shi, W., et al. (2013). Impacts of VIIRS SDR performance on ocean color products. *Journal of Geophysical Research: Atmospheres*, *118*, 10,347–10,360. https://doi.org/10.1002/jgrd.50793

Wang, M., & Shi, W. (2007). The NIR-SWIR combined atmospheric correction approach for MODIS ocean color data processing. *Optics Express*, *15*(24), 15722–15733. https://doi.org/10.1364/OE.15.015722

Wang, M., Shi, W., Jiang, L. D., & Voss, K. (2016). NIR- and SWIR-based on-orbit vicarious calibrations for satellite ocean color sensors. *Optics Express*, *24*(18), 20437–20453. https://doi.org/10.1364/OE.24.020437

Wang, M., Shi, W., & Tang, J. W. (2011). Water property monitoring and assessment for China's inland Lake Taihu from MODIS-Aqua measurements. *Remote Sensing of Environment*, *115*(3), 841–854. https://doi.org/10.1016/j.rse.2010.11.012

Wang, M., Son, S., & Shi, W. (2009). Evaluation of MODIS SWIR and NIR-SWIR atmospheric correction algorithms using SeaBASS data. *Remote Sensing of Environment*, *113*(3), 635–644. https://doi.org/10.1016/j.rse.2008.11.005

Wang, M., Son, S., & Harding, J. L. W. (2009). Retrieval of diffuse attenuation coefficient in the Chesapeake Bay and turbid ocean regions for satellite ocean color applications. *Journal of Geophysical Research*, *114*, C10011. https://doi.org/10.1029/2009JC005286

Wang, M., Tang, J. W., & Shi, W. (2007). MODIS-derived ocean color products along the China east coastal region. *Geophysical Research Letters*, *34*, L06611. https://doi.org/10.1029/2006GL028599

Wang, Y. P., Voulgaris, G., Li, Y., Yang, Y., Gao, J. H., Chen, J., & Gao, S. (2013). Sediment resuspension, flocculation, and settling in a macrotidal estuary. *Journal of Geophysical Research: Oceans*, *118*, 5591–5608. https://doi.org/10.1002/jgrc.20340

Wolanski, E., & Gibbs, R. J. (1995). Flocculation of suspended sediment in the Fly River estuary, Papua-New-Guinea. *Journal of Coastal Research*, *11*(3), 754–762.

Xi, H. Y., Larouche, P., Tang, S. L., & Michel, C. (2014). Characterization and variability of particle size distributions in Hudson Bay, Canada. *Journal of Geophysical Research: Oceans*, *119*, 3392–3406. https://doi.org/10.1002/2013JC009542

Erratum

Also, update the erratum statement to: The originally published version of this article included several minor typographical errors that were not corrected during publication. Additionally, the fifth sentence of section 3.4 incorrectly stated the range of η as ~−1.0 to −1.2, and the reference list entry for Gordon and Wang (1994) omitted its DOI. These errors have been corrected, and this may be considered the official version of record.